# $^{55}$Mn ENDOR of the $S_2$-State Multiline EPR Signal of Photosystem II: Implications on the Structure of the Tetranuclear Mn Cluster

**Jeffrey M. Peloquin,[†] Kristy A. Campbell,[†] David W. Randall,[‡] Marc A. Evanchik,[†] Vincent L. Pecoraro,[⊥] William H. Armstrong,[||] and R. David Britt*,[†]**

*Contribution from the Department of Chemistry, University of California, Davis, California 95616, Department of Chemistry, Stanford University, Stanford, California 94305, Department of Chemistry, University of Michigan, Ann Arbor, Michigan 48103-1055, and Department of Chemistry, Boston College, Chestnut Hill, Massachussetts 02167*

*Received June 12, 2000. Revised Manuscript Received September 5, 2000*

**Abstract:** We have performed continuous-wave electron paramagnetic resonance (CW-EPR) and electron spin echo electron nuclear double resonance (ESE-ENDOR) experiments on the multiline form of the $S_2$-state of untreated, MeOH-treated, and ammonia-treated spinach photosystem II (PS II) centers. Through simultaneously constrained simulations of the CW-EPR and ESE-ENDOR data, we conclude that four effective $^{55}$Mn hyperfine tensors ($A_X$, $A_Y$, $A_Z$) are required to properly simulate the experimental data [untreated and MeOH-treated PS II centers (MHz): −232, −232, −270; 200, 200, 250; −311, −311, −270; 180, 180, 240; ammonia-treated PS II centers (MHz): 208, 208, 158; −150, −150, −112; 222, 222, 172; −295, −315, −390]. We further show that these effective hyperfine tensors are best supported by a trimer/monomer arrangement of three Mn(IV) ions and one Mn(III) ion. In this topology, $Mn_A$, $Mn_B$, and $Mn_C$ form a strongly exchange coupled core ($J_{AB}$ and $J_{BC} < -100$ cm$^{-1}$) while $Mn_D$ is weakly exchange coupled ($J_{CD}$) to one end of the trinuclear core. For untreated and MeOH-treated PS II centers, the Mn(III) ion is either $Mn_A$ or $Mn_C$, with a zero-field-splitting of $D = -1.25$ to $-2.25$ cm$^{-1}$. For ammonia-treated PS II centers, the Mn(III) ion is $Mn_D$, with a zero-field-splitting of $D = +0.75$ to $+1.75$ cm$^{-1}$. The binding of the ammonia ligand results in a shift of the Mn(III) ion from the trinuclear core to the monomer Mn ion. This structural model can also account for the higher spin of the $g = 4.1$ signal and the magnetic properties of the $S_0$-state.

## Introduction

The oxygen evolving complex (OEC) of photosystem II (PS II) is the terminal electron donor to the photosynthetic cycle.[1,2] The OEC is not a separate isolatable protein complex, but rather its function depends on the relative intactness of the entire PS II protein complex. While no structure for the OEC has been determined, it is thought that the site of oxygen evolution is a cluster of four manganese ions ligated mainly by amino acid residues from the D1 protein. It is also thought that $Ca^{2+}$ and $Cl^-$ ions are part of the OEC. Recently, consensus has been forming that amino acid residues D1-Tyr161 and D1-His190 are intimately associated with the Mn ions and, therefore, could be considered part of the OEC as well.[3−8]

The Mn cluster acts to store intermediate oxidation equivalents generated by the photoinduced electron transfer in the PS II chlorophyll/pheophytin pigment array and also to position the substrate water molecules so as to facilitate the formation of the $O_2$ double bond upon their final oxidation. After four oxidation equivalents are transferred from the OEC, molecular oxygen is liberated, and the OEC resets to its most reduced state. The kinetic details of this oxygen evolving cycle were accurately modeled by Kok et al.,[9] and the cycle involving five so-called S-state intermediates ($S_{0-4}$) is referred to as the Kok or S-state cycle.

Although the kinetic, thermodynamic, and biochemical properties of the OEC have been extensively studied over the past 30 years,[2−4,10] much is still unknown about the detailed mechanism of oxygen evolution. To understand the mechanism, we need to have good insights into the OEC structure, and in particular, the structure of the Mn cluster at its core. In this paper, we present the results of high resolution $^{55}$Mn electron nuclear double resonance (ENDOR) experiments on the $S_2$-state of the cluster. The combination of the ENDOR spectroscopy, which measures the transition frequencies of the individual $^{55}$Mn nuclear spins of the cluster, in conjunction with electron paramagnetic resonance (EPR) spectral analysis, gives tightly constrained magnetic couplings for the individual $^{55}$Mn nuclei. We then consider the complementary information obtained from

[†] University of California.
[‡] Stanford University.
[⊥] University of Michigan.
[||] Boston College.

(1) Britt, R. D. In *Oxygenic Photosynthesis: The Light Reactions*; Ort, D., Yocum, C. F., Eds.; Kluwer Academic: Dordrecht, The Netherlands, 1996; pp 137−164.
(2) Debus, R. J. *Biochim. Biophys. Acta* **1992**, *1102*, 269−352.
(3) Hoganson, C. W.; Babcock, G. T. In *Metal Ions in Biological Systems*; Sigel, A., Sigel, H., Eds.; Marcel Dekker: New York, 2000; pp 613−656.
(4) Debus, R. J. In *Metal Ions in Biological Systems*; Sigel, A., Sigel, H., Eds.; Marcel Dekker: New York, 2000; pp 657−711.
(5) Peloquin, J. M.; Campbell, K. A.; Britt, R. D. *J. Am. Chem. Soc.* **1998**, *102*, 6840−6841.
(6) Dorlet, P.; Di Valentin, M.; Babcock, G. T.; McCracken, J. L. *J. Phys. Chem. B*, **1998**, *102*, 8239−8247.
(7) Lakshmi, K. V.; Eaton, S. S.; Eaton, G. R.; Frank, H. A.; Brudvig, G. W. *J. Phys. Chem. B* **1998**, *102*, 8327−8335.
(8) McLachlan, D. J.; Nugent, J. H. A. *Biochemistry* **1993**, *32*, 9772−9780.
(9) Kok, B.; Forbush, B.; McGloin, M. *Photochem. Photobiol.* **1970**, *11*, 457−475.
(10) Diner, B. A.; Babcock, G. T. In O*xygenic Photosynthesis: The Light Reactions*; Ort, D., Yocum, C. F., Eds.; Kluwer Academic: Dordrecht, The Netherlands, 1996; pp 213.

10.1021/ja002104f CCC: $19.00 
Published on Web 10/21/2000

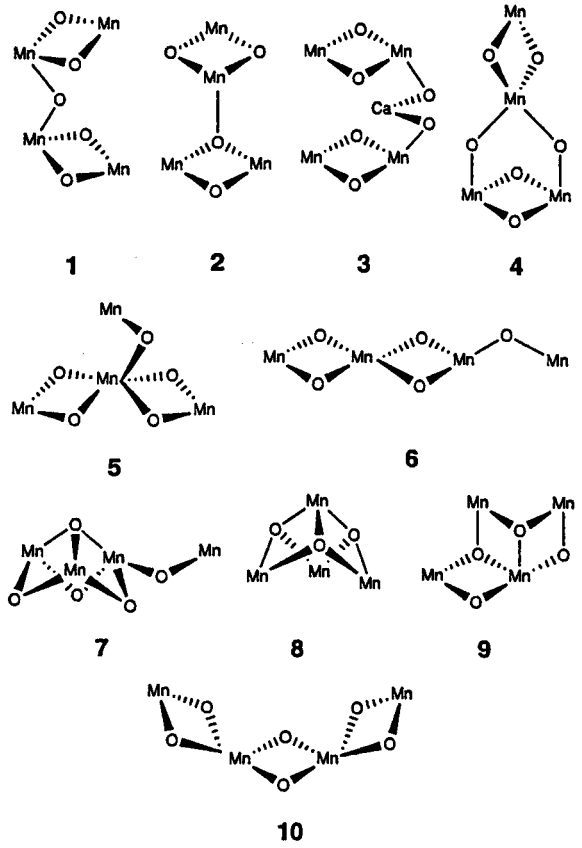


**Figure 1.** Tetranuclear structures of manganese ions relevant to the photosynthetic oxygen evolving complex that are consistent with EXAFS experiments. Reproduced with kind permission of Cinco et al.[68]

X-ray spectroscopic experiments (EXAFS and XANES) and develop a structural model for the Mn cluster that we consider to be consistent with the data from both the magnetic resonance and the X-ray experiments, as well as structural data from well-characterized Mn "model" clusters.

As mentioned, various X-ray absorption spectroscopic (XAS) techniques have provided much of the detailed information concerning the arrangement of these manganese ions.[11−15] Extended X-ray absorption fine structure (EXAFS) spectroscopy experiments provide evidence that in the $S_1$ and $S_2$ states, the manganese cluster contains two 2.7-Å Mn−Mn distances and one 3.3-Å Mn−Mn distance.[11,12,15] Figure 1 displays the proposed geometries considered by the Berkeley group to be consistent with their EXAFS data.[11] In all cases, the four manganese ions form a relatively compact tetranuclear cluster. X-ray absorption near edge absorption structure (XANES) spectroscopy supports a $S_1$-state valence assignment of Mn(III,III,IV,IV), with Mn(III,IV,IV,IV) in the $S_2$-state.[11,13−15]

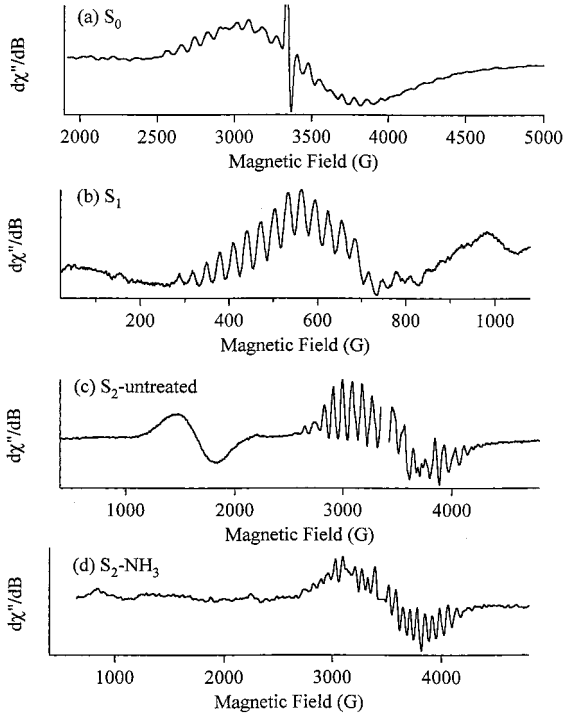


**Figure 2.** Comparison of the $^{55}$Mn hyperfine resolved EPR signal associated with the $S_0$, $S_1$, and $S_2$-states of the oxygen evolving complex. (a) $S_0$-state of 5% MeOH spinach PS II centers (reproduced with kind permission of Messinger et al.[33]); (b) $S_1$-state of *Synechocystis* PS II centers; (c) $S_2$-state of 3% MeOH spinach PS II centers; (d) $S_2$-state of ammonia-bound spinach PS II centers.

EPR spectroscopy provides another powerful tool for the study of the OEC.[1,5−7,16−22] EPR spectroscopy concerns itself with the absorption or emission of electromagnetic energy by the magnetic moments of atomic or molecular systems. These magnetic moments can either be of unpaired electrons alone in the case of EPR or both electrons and nuclei in the case of ENDOR. Figure 2 displays continuous-wave electron paramagnetic resonance (CW-EPR) signals from the first three S-states. Trace a shows the $g = 2$ "multiline" EPR signal of the $S_0$-state, observed with $^{55}$Mn hyperfine resolution only with added methanol. Trace b shows the parallel polarization EPR spectrum of the $S_1$-state. This integer spin state gives rise to resolved $^{55}$Mn hyperfine in cyanobacterial PS II preparations (as shown)[23] or plant PS II preparations when extrinsic proteins of MW 17 and 24 kDa have been removed.[24] Trace c shows the two well-characterized $S_2$-state signals, the $g = 2$ multiline signal, with approximately 18−21 resolved $^{55}$Mn hyperfine features, and the $g = 4.1$ signal, which shows no $^{55}$Mn hyperfine except in the case of certain oriented samples.[25−27] Ammonia incubation alters

(11) Yachandra, V. K.; Sauer, K.; Klein, M. P. *Chem. Rev.* **1996**, *96*, 2927−2950.
(12) Schiller, H.; Dittmer, J.; Iuzzolino, L.; Dörner, W.; Meyer-Klaucke, W.; Solé, V. A.; Nolting, H.-F.; Dau, H. *Biochemistry* **1998**, *37*, 7340−7350.
(13) Iuzzolino, L.; Dittmer, J.; Dörner, W.; Meyer-Klaucke, W.; Dau, H. *Biochemistry* **1998**, *37*, 17112−17119.
(14) Riggs, P. J.; Mei, R.; Yocum, C. F.; Penner-Hahn, J. E. *J. Am. Chem. Soc.* **1992**, *114*, 10650−10651.
(15) Penner-Hahn, J. E. In *Metal Sites in Proteins and Models: Redox Centres*; Hill, H. A. O., Sadler, P. J., Thomson, A. J., Eds.,; Springer: Berlin, 1998; pp 1−36.
(16) Randall, D. W.; Sturgeon, B. E.; Ball, J. A.; Lorigan, G. A.; Chan, M. K.; Klein, M. P.; Armstrong, W. H.; Britt, R. D. *J. Am. Chem. Soc.* **1995**, *117*, 11780−11789.
(17) Zheng, M.; Dismukes, G. C. *Inorg. Chem.* **1996**, *35*, 3307−3319.
(18) Hasegawa, K.; Kusunoki, M.; Inoue, Y.; Ono, T.-A. *Biochemistry* **1998**, *37*, 9457−9465.
(19) Hasegawa, K.; Ono, T.-A.; Inoue, Y.; Kusunoki, M. *Chem. Phys. Lett.* **1999**, *300*, 9−19.
(20) Åhrling, K. A.; Smith, P. J.; Pace, R. J. *J. Am. Chem. Soc.* **1998**, *120*, 13202−13214.
(21) Åhrling, K. A.; Pace, R. J. *Biophys J.* **1995**, *68*, 2081−2090.
(22) Messinger, J.; Nugent, J. H. A.; Evans, M. C. W. *Biochemistry* **1997**, *36*, 11055−11060.
(23) Campbell, K. A.; Peloquin, J. M.; Pham, D. P.; Debus, R. J.; Britt, R. D. *J. Am. Chem. Soc.* **1998**, *120*, 447−448.
(24) Campbell, K. A.; Gregor, W.; Peloquin, J. M.; Pham, D. P.; Debus, R. J.; Britt, R. D. *Biochemistry* **1998**, *37*, 5039−5045.
(25) Dismukes, G. C.; Siderer, Y. *Proc. Natl. Acad. Sci. U.S.A.* **1981**, *78*, 274−278.
(26) Casey, J. L.; Sauer, K. *Biochem Biophys Acta* **1984**, *767*, 21−28.
(27) Kim, D. H.; Britt, R. D.; Klein, M. P.; Sauer, K. *Biochemistry* **1992**, *31*, 541−547.

the $g = 2$ multiline signal under conditions of ammonia ligation to the Mn cluster, as shown in trace d.[28,29] Additionally, certain inhibitor treatments give rise to an $S_2-Y_Z^{\bullet}$ "interaction" spectrum (not shown) that has provided much information concerning the magnetic interaction between the Mn cluster and the crucial $Y_Z^{\bullet}$ tyrosine radical.[5−8]

**Interpretation of EPR and ENDOR Spectra.** Equation 1 is the general spin Hamiltonian for a system containing *n* electron and *n* nuclear magnetic moments, such as the case for *n* Mn paramagnetic ions, each with an associated magnetic ($^{55}$Mn) nucleus.[30]

$$\hat{H}_{\text{uncoupled}} = \sum_{i}^{n}[\vec{B}\cdot\tilde{g}_i\cdot\hat{S}_i + \hat{S}_i\cdot\tilde{A}_i\cdot\hat{I}_i + \hat{S}_i\cdot\tilde{D}_i\cdot\hat{S}_i + \hat{I}_i\cdot\tilde{P}_i\cdot\hat{I}_i - \gamma_i\hat{B}\cdot\mathrm{I}_i] - \sum_{\substack{j,k \\ j\neq k}}^{n} J_{jk}\hat{S}_j\cdot\hat{S}_k \quad (1)$$

The first term is the electron Zeeman term. The second term is the electron−nuclear hyperfine term where, in this case, we are neglecting hyperfine interactions with nuclei other than the one directly associated with the *i*th electron spin. The third term is the electronic zero-field-splitting term. The fourth term is the nuclear quadrupole zero-field-splitting term. The fifth term is the nuclear Zeeman term. The final term represents the magnetic exchange couplings between the *n* paramagnetic ions, assumed to be isotropic in this work. In this equation, $\vec{B}$ is the external magnetic field; $\tilde{g}_i$ is the **g**-tensor of atom *i*; $\hat{S}_i$ is the electron spin angular momentum operator associated with the electron magnetic moment of atom *i*; $\hat{I}_i$ is the nuclear spin angular momentum operator associated with the nuclear magnetic moment of nucleus *i*; $\hat{A}_i$ is the hyperfine tensor for the interaction of the electron magnetic moment of atom *i* with the nuclear magnetic moment of nucleus *i*; $\hat{P}_i$ is the quadrupole tensor of nucleus *i*; $\gamma_i$ is the gyromagnetic ratio of nucleus *i*.

The exchange couplings between the *n* ions correlate their spins. This leads to a ladder of total "coupled" spin states ($S_T$), which results as a vector sum of the individual ion spin vectors.[31] For a given coupled spin state, one can rewrite eq 1 in terms of a total spin angular momentum operator $\hat{S}_T$, as shown in eq 2:

$$\hat{H}_{\text{coupled}} = \vec{B}\cdot\tilde{g}'\cdot\hat{S}_T + \sum_{i}^{n}[\hat{S}_T\cdot\tilde{A}_i'\cdot\hat{I}_i + \hat{I}_i\cdot\tilde{P}_i\cdot\hat{I}_i - \gamma_i\vec{B}\cdot\hat{I}_i] + \hat{S}_T\cdot\tilde{D}'\cdot\hat{S}_T \quad (2)$$

For this spin state, there is a $\tilde{g}'$ matrix associated with the coupled spin state $S_T$, along with a zero-field-splitting matrix, $\tilde{D}'$, if the total spin, $S_T$, is one or greater. This total spin, $S_T$, interacts with the *n* individual nuclei through a set of hyperfine matrices $\tilde{A}_i'$. Additionally, each nucleus has a quadrupolar coupling and a nuclear Zeeman term, the same as in the uncoupled case.

The details of the ladder of spin states and the vector couplings that define them depend on the number of paramagnetic ions, their individual spins, and the pattern of exchange couplings between the ions. For example, antiferromagnetic coupling ($J_{12} < 0$) between an $S = 2$ Mn(III) ion and an $S = {}^3/_2$ Mn(IV) ion of a Mn(III,IV) dinuclear cluster leads to four distinct total spin states, $S_T = |S_{III} - S_{IV}|$ .. $|S_{III} + S_{IV}| = {}^1/_2$, ${}^3/_2$, ${}^5/_2$, and ${}^7/_2$, with $S_T = {}^1/_2$ being the ground spin state. The difference in energy between the ground $S = {}^1/_2$ state and the first excited $S = {}^3/_2$ state is equal to $3J_{12}$. The order of the ladder is reversed for ferromagnetic coupling ($J_{12} > 0$).

The coupled **g**-tensor, $\tilde{g}'$, the zero-field-splitting tensor, $\tilde{D}'$, and the hyperfine tensors, $\tilde{A}'$, in eq 2 are not identical to the tensors in the uncoupled representation (eq 1) and are referred to as "effective tensors" for the coupled state. For example, the relationship between a given effective hyperfine tensor, $\tilde{A}_i'$, and the intrinsic tensors, $\tilde{A}_i$ (in eq 2), of the isolated, uncoupled ions (in eq 1) is given by a so-called projection matrix $\rho$, which depends on the total spin state $S_T$, the isolated spins $S_i$, and their respective zero-field-splitting tensors $\tilde{D}_i$, and the pattern of exchange interactions $J_{jk}$ ($\tilde{A}_i' = \tilde{A}_i\cdot\rho(S_T, J_{jk}, \tilde{D}_i)$). Calculation of the projection matrix follows the quantum mechanical rules for addition of angular momenta in a straightforward fashion.[31] In a similar fashion, the coupled $\tilde{g}'$ and $\tilde{D}'$ matrices can be related to the isolated $\tilde{g}_i$ and $\tilde{D}_i$ matrices through comparable projection matrices. Each individual total spin state of the system will have a different set of projection matrices, and as a result, a different set of effective $\tilde{g}'$, $\tilde{A}'$, and $\tilde{D}'$ tensors.

In summary, eq 1 is referred to as the uncoupled spin Hamiltonian because the individual spin operators are present, while eq 2 is referred to as the coupled spin Hamiltonian because the individual spin operators are coupled into the total spin operator. The coupled Hamiltonian can be considered the observed Hamiltonian because the applied microwave radiation in an EPR or ENDOR experiment interacts with the total magnetic moment of a spin system, and it is therefore the $\tilde{g}'$, $\tilde{A}'$, and $\tilde{D}'$ tensors that are measured. As a result, an EPR or ENDOR spectrum is first analyzed in terms of eq 2, and then the effective tensors can be transformed to the corresponding intrinsic tensors through calculation of the projection matrices.

Conventional CW-EPR spectroscopy is usually adequate for determining the effective $\tilde{g}'$ and $\tilde{D}'$ tensors in eq 2. In cases where the majority of the allowed EPR transitions are resolved, CW-EPR can determine the effective hyperfine tensors. In cases of high spectral congestion, such as the case for the PS II Mn signals (Figure 2), the ENDOR technique provides a much better measure of the effective hyperfine tensors and also of the nuclear quadrupole tensors, which are typically difficult to extract from CW-EPR spectra. For systems with $S_T = {}^1/_2$, the effective zero-field-splitting term, $\tilde{D}'$, is zero. However, the intrinsic $\tilde{D}_i$ tensors still influence the hyperfine projection matrices relating the intrinsic and effective hyperfine matrices; therefore these $\tilde{D}_i$ matrices can be probed via ENDOR.

Since the first observation of the $g = 2$ multiline CW-EPR signal of the $S_2$-state of the OEC, numerous EPR spectral analyses have been performed. Table 1 lists the results of a number of recent simulations of the $g = 2$ multiline signal (Figure 2, trace c) using a coupled spin Hamiltonian similar to eq 2. As can be seen, it is possible to fit the CW-EPR spectrum with a variety of effective $^{55}$Mn hyperfine couplings. While the majority of researchers propose that all four manganese ions contribute to the EPR spectrum, Åhrling et al. have proposed that the EPR signals of the $S_2$-state arise from a Mn(III)−Mn(III) dimer interacting with a ligated organic radical, presumably a histidine or tyrosine amino acid residue.[20,21]

It is clear from the diversity of simulation parameters summarized in Table 1 that the use of CW-EPR spectroscopy alone has not led to a unique magnetic model of the manganese

(28) Beck, W. F.; de Paula, J. C.; Brudvig, G. W. *J. Am. Chem. Soc.* **1986**, *108*, 4018−4022.
(29) Britt, R. D.; Zimmerman, J. L.; Sauer, K.; Klein, M. P. *J. Am. Chem. Soc.* **1989**, *111*, 3522−3532.
(30) Abragam, A.; Bleaney, B. *Electron Paramagnetic Resonance of Transitions Ions*; Dover: New York, 1970.
(31) Bencini, C.; Gatteschi, D. *EPR of Exchange Coupled Systems*; Springer-Verlag: Berlin, 1990.

**Table 1.** $^{55}$Mn Hyperfine Tensors for the $S_2$-State Multiline CW-EPR Signal Predicted by Other Researchers

| model (ref) | $Mn_A$ $A'_X, A'_Y, A'_Z$ (MHz) | $Mn_B$ $A'_X, A'_Y, A'_Z$ (MHz) | $Mn_C$ $A'_X, A'_Y, A'_Z$ (MHz) | $Mn_D$ $A'_X, A'_Y, A'_Z$ (MHz) | oxidation states |
|---|---|---|---|---|---|
| Zheng and Dismukes 1996[17] | 237, 237, 237 | 237, 237, 237 | −257, −257, −337 | −280, −280, −300 | 1(III),3(IV) |
| Zheng and Dismukes 1996[17] | −277, −277, −363 | −277, −277, −363 | 226, 226, 288 | 250, 250, 226 | 3(III),1(IV) |
| Hasegawa et al.[18,19] 1999 | 248, 232, 245 | 291, 284, 194 | 110, 106, 117 | 294, 304, 294 | 1(III),3(IV) |
| Lakshmi et al.[49] 1999 | 207, 207, 261 | 251, 251, 266 | 251, 251, 266 | 251, 251, 266 | 1(III),3(IV) |
| Åhrling et al. 1995[20] | 548, 650, 174 | −263, −367, −140 | | | 2(III) + radical |
| quadrupole | −21.3, −28, 49.3 | 51.2, −26.9, −24.4 | | | |

cluster. At least in part, this arises from the fact that the CW-EPR spectrum of a $S = {}^1/_2$ electron spin magnetically coupled to four $I = {}^5/_2$ $^{55}$Mn nuclei consists of 1296 different electron spin transitions. Because of spectral congestion, the multiline CW-EPR spectrum (Figure 2c) consists of only 18−21 features with line widths approaching 100 MHz, making an unique analysis of this underdetermined system practically impossible.

Although there are 1296 distinct allowed EPR transitions for a tetranuclear Mn cluster, there are only 40 distinct allowed $^{55}$Mn nuclear spin transitions. Therefore, one would expect a large decrease in spectral congestion if one could measure the NMR spectra of the $^{55}$Mn nuclei. For the paramagnetic $S_2$-state, this can be done with high sensitivity using ENDOR methods. Therefore, to overcome the limitations of CW-EPR spectroscopy, we have performed a series of pulsed ENDOR experiments on the $S_2$-state forms of the OEC to measure the $^{55}$Mn nuclear spin transition frequencies. A key benefit in the use of ENDOR spectroscopy is the fact that any magnetic model of the manganese cluster must be able to reproduce the ENDOR spectra as well as the CW-EPR spectra. This need to fit both experimental observables with the same spin Hamiltonian parameters results in very tight constraints for any proposed structural model. We have shown in previous reports that for a given magnetic field position, electron spin echo electron nuclear double resonance (ESE-ENDOR) resolves three $^{55}$Mn features with widths of approximately 15−20 MHz,[5,16] but we have to date provided little discussion as to how our ESE-ENDOR data can be used to construct a structural model of the tetramanganese cluster of PS II.[5,16]

Here, we report a full ESE-ENDOR characterization of untreated, MeOH-treated, and ammonia-treated spinach PS II centers trapped in the $S_2$-state. We discuss the validity of previously reported structural models for the manganese cluster of the OEC in terms of these new ENDOR data. Through simultaneous spectral simulations of both the CW-EPR and ENDOR data, we demonstrate that four manganese hyperfine tensors are needed to properly simulate the data. We further are able to use a single tetranuclear structural model for the manganese cluster, consisting of a strongly exchange coupled trinuclear Mn core with a flanking weakly exchange coupled fourth Mn ion, to support the effective $^{55}$Mn hyperfine tensors used to simulate the CW-EPR and ENDOR data of untreated, MeOH-treated, and ammonia-treated PS II centers. Although we do not have $^{55}$Mn ENDOR spectra at this time for the $S_2$-state $g = 4.1$ signal or the $S_0$-state $g = 2$ multiline signal, this same structural model describes the magnetic properties of those states as determined by CW-EPR.[32,33] Additionally, the model is fully consistent with Mn−Mn distances and oxidation states as determined by X-ray spectroscopies[11−15] and with exchange coupling parameters measured in well-characterized Mn "model" clusters.

## Materials and Methods

**Sample Preparation.** The model compounds $[(phen)_2Mn(III)O_2Mn(IV)(phen)_2)](ClO_4)_3$ (compound A) and $(Mn(III)Mn(IV)[$ 2-OH-3,5-$Cl_2$-(salpn)$]_2(THF)(ClO_4)$ (compound B) were prepared as previously described.[16,34,35] PS II membrane particles were isolated using the "BBY" membrane isolation method[36] as modified in Campbell et al.[24] Samples were resuspended in a buffer containing 5 mM $CaCl_2$, 15 mM $MgCl_2$, 10 mM NaCl, 400 mM sucrose, and either (i) 50 mM MES (pH 6.0) with 0 or 3% (v/v) methanol or (ii) 50 mM HEPES (pH 7.5) and 100 mM ammonia chloride. For EPR measurements, samples were concentrated to greater than 20 mg/mL Chl and loaded in 3.8-mm OD quartz EPR tubes. Untreated and MeOH-treated PS II samples were trapped in the $S_2$-state by 5 min illumination at 200 K. Ammonia-treated samples were trapped in an altered $S_2$-state by 5 min illumination at 200 K followed by a 30 s annealing at 0 °C to allow for binding of the ammonia to the manganese cluster with the concomitant alteration of the CW-EPR line shape.[29] Following collection of the ESE-ENDOR data on the illuminated samples trapped in the various $S_2$-state form, the samples were poised in the dark stable $S_1$-state by 1 h dark adaptation at 0 °C. The ESE-ENDOR spectra of the $S_1$-states were subsequently acquired, and these dark spectra were then subtracted from the illuminated spectra to give light-minus-dark ENDOR spectra that correspond only to the light-induced $S_2$-state multiline EPR signal, with any background ENDOR signals negated by the subtraction.

**EPR Spectroscopy.** CW-EPR spectra were recorded on a Bruker ECS106 X-band CW-EPR system with a Bruker ER 4116DM dual mode cavity capable of both parallel (TE012) and perpendicular (TE102) mode polarizations of the applied magnetic field. Cryogenic temperatures were obtained with an Oxford ESR900 helium cryostat. The temperature was controlled with an Oxford ITC503 temperature and gas flow controller.

The ESE-ENDOR experiments were performed with an instrument of our own design[37,38] using the Davies ESE-ENDOR pulse sequence ($\pi - T - \pi/2 - \tau - \pi - \tau -$ ESE),[39] where $\pi$ and $\pi/2$ refer to the electron magnetization flip angles driven by the microwave pulses, and the time intervals of $T$ and $\tau$ were chosen to maximize the ESE-ENDOR signal. The RF radiation to drive the $^{55}$Mn nuclear spin flips was applied during the $T$ time interval.

**Spectral Simulations.** All CW-EPR and ESE-ENDOR data were simulated with the coupled spin Hamiltonian given by eq 2. For simulations with only two $I = {}^5/_2$ $^{55}$Mn nuclei, the eigenvalues and eigenvectors were determined through full matrix diagonalization of the 72 × 72 Hamiltonian matrix for a coupled $S = {}^1/_2$, two $I = {}^5/_2$ spin system. For simulations requiring three or more $^{55}$Mn nuclei, the eigenvalues and eigenvectors were calculated using the separate diagonalization method described in Appendix 1.

In the CW-EPR simulations, the transition probabilities of all electron spin transitions in resonance with the microwave frequency are calculated. The allowed electron spin transitions are broadened with a 15 G Gaussian line shape function. In the ESE-ENDOR simulations,

(32) Boussac, A.; Girerd, J.-J.; Rutherford, A. W. *Biochemistry* **1996**, *35*, 6984−6989.

(33) Messinger, J.; Robblee, J. H.; Yu, W. O.; Sauer, K.; Yachandra, V. K.; Klein, M. P. *J. Am. Chem. Soc.* **1997**, *119*, 11349−11350.

(34) Randall, D. W.; Chan, M. K.; Armstrong, W. H.; Britt, R. D. *Mol. Phys.* **1998**, *95*, 1283−1294.

(35) Larson, E.; Haddy, A.; Kirk, M. L.; Sands, R. H.; Hatfield, W. E.; Pecoraro, V. L. *J. Am. Chem. Soc.* **1992**, *114*, 6263−6265.

(36) Berthold, D. A.; Babcock, G. T.; Yocum, C. F. *FEBS Lett* **1981**, *134*, 231−234.

(37) Sturgeon, B. E.; Britt, R. D. *Rev. Sci. Instrum.* **1992**, *63*, 2187.

(38) Sturgeon, B. E.; Ball, J. A.; Randall, D. W.; Britt, R. D. *J. Phys. Chem.* **1995**, *98*, 12871−12883.

(39) Davies, E. R. *Phys. Lett.* **1974**, *47A*, 1−2.

**Table 2.** Standard Intrinsic $^{55}$Mn(III) and $^{55}$Mn(IV) Hyperfine Tensors

| ion | $A_X$ | $A_Y$ | $A_Z$ | $A_{iso}$ | $A_{dip}$ |
|---|---|---|---|---|---|
| $^5A_1$ Mn(III) | −213 | −213 | −159 | −165 to −225 | 10 to 20 |
| $^5B_{1g}$ Mn(III) | −177 | −177 | −229 | −165 to −225 | −10 to −20 |
| Mn(IV) | −220 | −220 | −220 | −187 to −253 | −9 to +9 |

all electron spin transitions in resonance with the microwave frequency within a Gaussian width of 25 MHz are determined for the specified magnetic field position. For these allowed electron spin transitions, the allowed nuclear spin transition frequencies and corresponding transition probabilities are calculated. These nuclear transition probabilities are multiplied by the transition probability of the appropriate electron spin transition and broadened with a 3-MHz line shape function.

Table 2 lists a set of standard intrinsic hyperfine tensors for Mn(III) and Mn(IV) ions. The listed tensors were compiled from a number of published reports.[16,17,34,40−42] Columns 5 and 6 show the expected ranges of the isotropic and dipolar portions of the hyperfine tensors for each ion, where $A_{iso} = (A_X + A_Y + A_Z)/3$ and $A_{dip} = (A_Z - (A_X + A_Y)/2)/3$. Columns 2−4 list the average tensor components for each ion based on the ranges in columns 5 and 6. We list two different sets of parameters for the Mn(III) ions because the two different possible ground-state electronic configurations, $^5A_1$ and $^5B_{1g}$, have different signs for the dipolar portion of the hyperfine tensor.

In all the simulations presented in this paper, we assume that the principal axes of the various tensors are all collinear. Given the fact that the coupled spin Hamiltonian for the manganese cluster contains nine different tensor quantities, all of which have three angular degrees of freedom, insufficient experimental data exist at this point to support a full free parameter approach. However, we are currently pursuing ESE-ENDOR experiments on oriented PS II systems to address further experimentally the question of relative tensor orientation.

## Results

**Dinuclear Manganese Compounds.** We begin by characterizing $^{55}$Mn ENDOR spectra of structurally determined dinuclear "model" clusters. This then serves as a basis for examining the ENDOR spectra of the $S_2$-state. Figure 3 shows the first derivative ESE-EPR field swept and ESE-ENDOR spectra for two different dinuclear Mn compounds along with simulations (dashed lines). Compound A[34] is $[(phen)_2Mn(III)O_2Mn(IV)(phen)_2)](ClO_4)_3$, and compound B[35] is $(Mn(III)Mn(IV)[2\text{-}OH\text{-}3,5\text{-}Cl_2\text{-}(salpn)]_2(THF)(ClO_4)$. We have previously published simulations of the ESE-EPR and ESE-ENDOR data of compound A using eq 2.[34] These simulations were performed using full matrix diagonalization of the Hamiltonian matrix. The parameters used in the simulations are shown in Table 3. We have also acquired and simulated the ESE-EPR and ESE-ENDOR data for compound B, again using eq 2 and full matrix diagonalization. The parameters used in these simulations are also included in Table 3. While we are able to simulate the compound A data quite well, there is still a small mismatch between the experimental and the simulated spectra for compound B. Our simulation parameters for compound B are quite different from those reported by Zheng et al.[41] This difference is not unexpected because Zheng et al. report they did not have access to the actual CW-EPR experimental data with which to perform their simulation.

Our current simulation includes a fairly large rhombicity for the compound B **g**-tensor ($g_x = 1.88$, $g_y = 1.99$, $g_z = 2.01$).

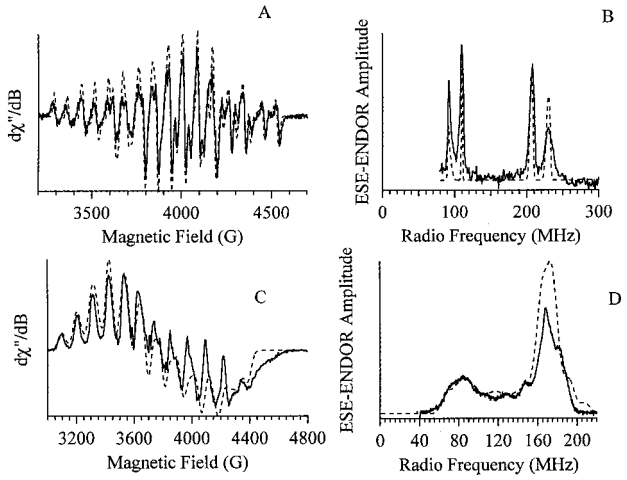


**Figure 3.** (A) First derivative of ESE-EPR field swept spectrum of compound A ($[(phen)_2Mn(III)O_2Mn(IV)(phen)_2)](ClO_4)_3$); (B) ESE-ENDOR spectrum of compound A at $H = 3966$ G; (C) First derivative of ESE-EPR field swept spectrum of compound B ($(Mn(III)Mn(IV)\text{-}[2\text{-}OH\text{-}3,5\text{-}Cl_2\text{-}(salpn)]_2(THF)(ClO_4)$); (D) ESE-ENDOR spectrum compound B at 4030 G. Experimental conditions: microwave frequency: (A and B) 10.955 GHz, (C and D) 10.362 GHz; tau: (A) 150 ns, (B) 210 ns, (C) 350 ns, (D) 300 ns; $\pi/2$ MW pulselength: (A, B, and D) 15 ns, (C) 100 ns; MW power: (A, B, and D) 50 W (C) 2 mW; RF power (B and D) 100 W; RF pulselength: (B) 20 $\mu$s, (D) 4.5 $\mu$s; repetition rate: (A and B) 200 Hz, (C and D) 500 Hz.

**Table 3.** Simulation Parameters for Compounds A and B[a]

| ion | $A_X$ | $A_Y$ | $A_Z$ |
|---|---|---|---|
| (A) Mn(III) | −480 | −480 | −360 |
| (A) Mn(IV) | 212 | −212 | −231 |
| (B) Mn(III) | −330 | −330 | −350 |
| (B) Mn(IV) | 140 | 140 | 310 |

[a] Compound A: $g_x = 1.995$, $g_y = 1.995$, $g_z = 1.982$. Compound B: $g_x = 1.88$, $g_y = 1.99$, $g_z = 2.01$.

This rhombicity may arise as an artifactual consequence of our assumption that the **g**-tensor is collinear with the hyperfine tensors. Following a 90° rotation of the **g**-tensor *z*-axis relative to the hyperfine tensor *z*-axis, we recover a **g**-tensor with less rhombicity ($g_x = 2.01$, $g_y = 1.99$, $g_z = 1.88$). We are currently performing simulations of the EPR and ENDOR spectra of compound B in which no restrictions are placed on the relative alignments of the individual tensor components. This more sophisticated analysis should remove the discrepancy that exists between the experimental data and the calculated spectra in Figure 3C,D for compound B. Such noncollinearity of the tensors has been observed by Schäfer et al. in a number of Mn(III,IV) compounds.[42]

Although both compounds A and B are Mn(III,IV) dinuclear complexes, it is clear that the effective $^{55}$Mn hyperfine tensors are drastically different. The difference in the effective $^{55}$Mn hyperfine tensors can be easily explained in terms of the bridges that mediate the antiferromagnetic exchange coupling within the dinuclear units of the two complexes. In compound A, two di-$\mu$-oxo bridges link the two manganese ions with a Mn−Mn distance of ≈2.72 Å.[16] In compound B, a single dimethoxy bridge links the two manganese ions with a Mn−Mn distance of ≈3.65 Å.[35] In both compounds, the bridging oxygens allow the atomic orbitals of the individual manganese ions to interact with one another, leading to a nonzero exchange interaction, $H_{ex}$, between the electrons of the Mn(III) ion and the electrons of the Mn(IV) ions. This exchange interaction can be written in terms of the electron spin angular momentum operators as $H_{ex} = -J_{jk}\hat{S}_j \cdot \hat{S}_k$. Since the exchange interaction is mediated by

(40) Randall, D. W. Pulsed EPR Studies of Tyrosine Radicals and Manganese Complexes: Insight into Photosynthetic Oxygen Evolution, Ph.D. Dissertation, University of California, Davis, 1997.

(41) Zheng, M.; Khangulov, S. V.; Dismukes, G. C.; Barynin, V. V. *Inorg. Chem.* **1994**, *33*, 383−387.

(42) Schäfer, K.-O.; Bittl, R.; Zweygart, W.; Lendzian, F.; Haselhorst, G.; Weyhermüller, T.; Wieghardt, K.; Lubitz, W. *J. Am. Chem. Soc.* **1998**, *120*, 13104−13120.

the nature of the overlap of the atomic orbitals of the oxygen with the atomic orbitals of the manganese ions, the value of $J$ depends on the geometry of the dinuclear unit. Magnetic susceptibility experiments show that $J = -150$ cm$^{-1}$ for the short bridge of compound A and $-10$ cm$^{-1}$ for the long bridge of compound B.[34,35]

Although compounds A and B have different bridging units, there is very little significant difference in the ligand environment of the manganese ions in either complex, and the Mn(III) and Mn(IV) ions in both complexes should have very similar intrinsic $^{55}$Mn hyperfine tensors. We can therefore conclude then that the difference in the effective $^{55}$Mn hyperfine tensors for compounds A and B must arise from differences in exchange couplings and their manifestations on the projection matrices, $\rho(J,D,S)$. Equation 3 is a second-order perturbation equation for the projection matrices of a dinuclear Mn(III,IV) complex in terms of the exchange interaction, $J$, and the axial zero-field-splitting term, $D$.[34,41,43]

$$\rho_{III} = 2 + \frac{2}{5J}(7\tilde{D}_{III} + 2\tilde{D}_{IV})$$
$$\rho_{IV} = -1 - \frac{2}{5J}(7\tilde{D}_{III} + 2\tilde{D}_{IV}) \quad (3)$$

For a Mn(III) ion and Mn(IV) ion, the values of the axial zero-field-splittings are $|D_{III}| = 1-4$ cm$^{-1}$ and $|D_{IV}| = 0.1-0.4$ cm$^{-1}$, respectively. Since compound A has an exchange coupling, $J$, much larger than $D$ whereas compound B has an exchange coupling, $J$, of the same order of magnitude as $D$, it is clear that the two complexes should have very different projection matrices and, therefore, different effective $^{55}$Mn hyperfine tensors. The small value of $J$ for compound B leads to a $\approx$30 cm$^{-1}$ difference between the $S = {}^1/_2$ ground spin state and $S = {}^3/_2$ first excited spin state of the systems. This energy separation is small enough that the zero-field-splitting term mixes appreciable $S = {}^3/_2$ excited-state character into the $S = {}^1/_2$ ground state.

Figure 4 shows the $D_{III}$ dependence of the intrinsic $A_{iso}$ (thick solid line) and $A_{dip}$ (thin solid solid) values for the Mn(III) and Mn(IV) ions calculated using the projection matrix expressions (eq 3) and the appropriate measured effective hyperfine matrices (Table 2) Because the zero-field-splitting of the Mn(IV) ion is much smaller than that of the Mn(III) ion, it does not contribute to the calculation, and we approximate $D_{IV} = 0$ cm$^{-1}$. The thin dashed lines in Figure 4 represent the expected range of the intrinsic $^{55}$Mn hyperfine tensors derived from the studies of a number of model Mn(III,IV) compounds as shown in Table 2 (see Materials and Methods). We see for compound A, with its strong antiferromagnetic coupling, that this approach offers no discrimination; the calculated values are acceptable over a wide range of $D_{III}$ values. The calculated intrinsic tensors for compound B clearly do depend on $D_{III}$. From Figure 4, the calculated values of the dipolar portion of the intrinsic $^{55}$Mn hyperfine tensors for compound B are within the expected range shown by the dashed lines only for values of $D_{III} = -2.5$ to $-3.8$, which is an acceptable range for a Mn(III) ion.

This simple study of dinuclear complexes illustrates a number of important points. First, the ESE-ENDOR spectra in Figure 3 clearly demonstrate that we are capable of distinguishing broad, weak signals above the background noise of our system. The effective anisotropy in the Mn(IV) hyperfine tensor of compound B is approximately nine times larger than the tensor in compound A, and therefore the line width is much greater.

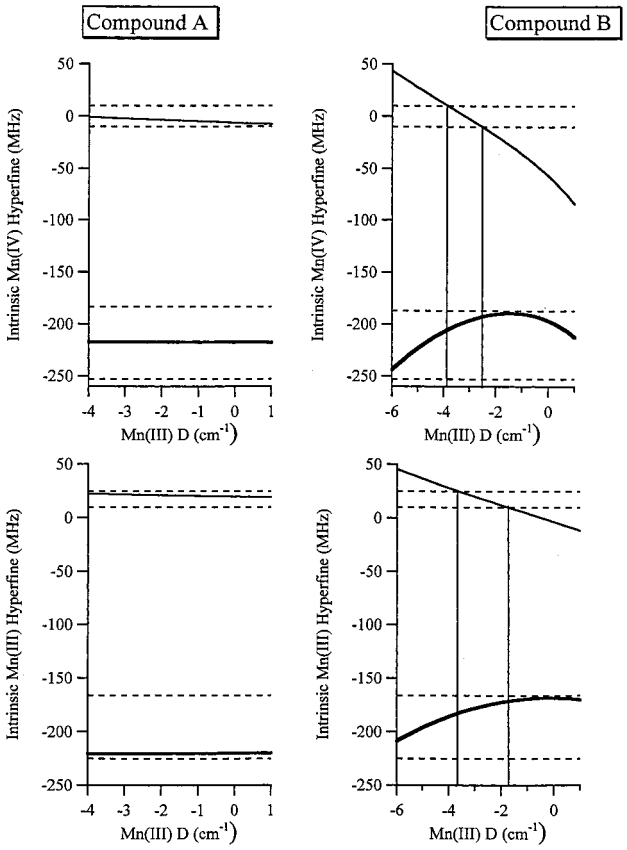


**Figure 4.** Plot of Intrinsic $^{55}$Mn hyperfine tensors versus D for $[(phen)_2Mn(III)O_2\ Mn(IV)(phen)_2)](ClO_4)_3$ (compound A) and (Mn(III)Mn(IV)[2-OH-3,5-Cl$_2$-(salpn)]$_2$(THF)(ClO$_4$) (compound B). The solid thick line represents the $A_{iso}$ portion of the intrinsic $^{55}$Mn hyperfine tensors. The thin solid line represents the $A_{dip}$ portion of the intrinsic $^{55}$Mn hyperfine tensors. The dashed lines represent the expected range for the $A_{iso}$ and $A_{dip}$ portions of the intrinsic $^{55}$Mn hyperfine tensor taken from Table 2.

Second, this analysis demonstrates the importance of taking into account the zero-field-splitting tensors of Mn(III) ions in determining the projection factors when the ground and first excited spin states are not well separated. This last point is of particular relevance to the analysis of the EPR data for the manganese cluster of PS II because it has been experimentally shown in the S$_2$-state that the first excited spin state is only 30$-$40 cm$^{-1}$ above the ground spin state.[1,44$-$46] This energy separation is small enough to allow the zero-field-splitting tensor of a Mn(III) ion to have a significant effect on the projection factors. Although both Hasegawa et al. and Zheng and Dismukes have proposed structures for the manganese cluster based on analysis of the CW-EPR spectra of the S$_2$-state, neither group included the effect of the Mn(III) zero-field-splitting in their calculations of projection factors. Third, we have demonstrated a capability of doing a thorough EPR/ENDOR simulation and analysis, using full matrix diagonalization methods, of dinuclear Mn complexes, which gives us confidence in our evaluation of any dinuclear Mn models for the S$_2$-state.

**PS II: The S$_2$-State of the OEC.** We now turn to the multiline EPR signal of the S$_2$-state of the PS II OEC. In particular, we examine the S$_2$-state EPR/ENDOR spectra of untreated PS II membranes, as well as those of membranes

(43) Sage, J. T.; Xia, Y.-M.; Debrunner, P. G.; Keough, D. T.; De Jersey, J.; Zerner, B. *J. Am. Chem. Soc.* **1989**, *111*, 7239$-$7247.

(44) Lorigan, G. A.; Britt, R. D. *Biochemistry* **1994**, *33*, 12072.

(45) Pace, R. J.; Smith, P.; Bramley, R.; Stehlik, D. *Biochim. Biophys. Acta* **1991**, *1058*, 161$-$170.

(46) Hansson, O. A.; R. Vängård, T. *Biophys J.* **1987**, *51*, 825$-$832.

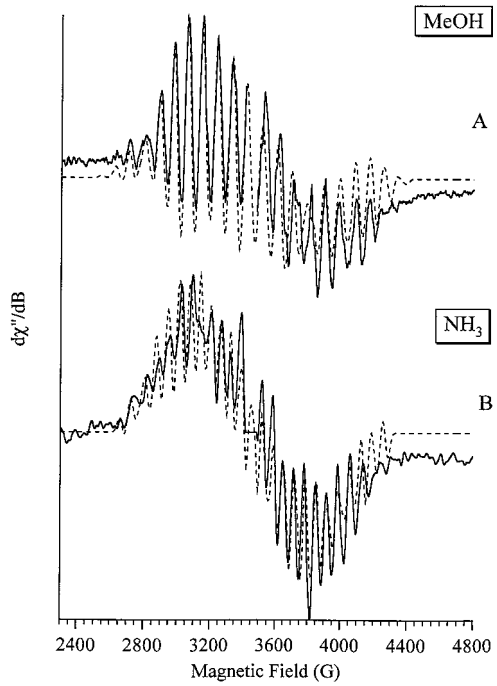


**Figure 5.** (A) Light-minus-dark CW-EPR difference spectra of 3% MeOH-treated spinach PS II centers (solid line) and spectral simulation (dashed lined). (B) Annealed-minus-dark CW-EPR spectra of 100 mM $NH_4Cl$-treated spinach PS II centers (solid line) and spectral simulation (dashed line). Experimental conditions: microwave frequency: (A) 9.680 GHz, (B) 9.670 GHz; microwave power = 3.2 mW; modulation amplitude = 10G; modulation frequency = 100 kHz; time constant = 40.96 ms; conversion time = 81.92 ms; temperature = 7 K.

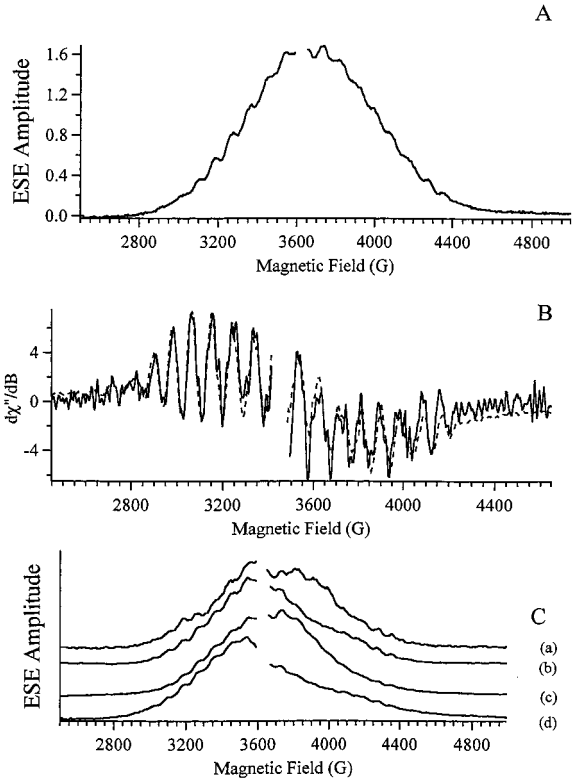


**Figure 6.** (A) $S_2-S_1$ difference ESE-EPR field swept spectrum of MeOH-treated PS II centers using long, selective microwave pulses. (B) Comparison of the first derivative of trace A (solid line) with the $S_2-S_1$ difference CW-EPR spectrum MeOH-treated PS II centers from Figure 5A (dashed line). (C) Comparison of $S_2-S_1$ difference ESE-EPR field swept spectra of MeOH-treated PS II centers using short, nonselective microwave pulses at four different values of $\tau$, (a) 600 ns, (b) 210 ns, (c) 195 ns, (d) 150 ns; experimental conditions: microwave frequency = 10.151 GHz; $\pi/2$ microwave pulse length = (A) 100 ns; (B and C) 15 ns; $\tau$ = (A) 400 ns; (C) see above; microwave power = (A) 0.5 W; (B) 30 W; repetition time = 5 ms, temperature = 4.24 K.

treated with 3% methanol (denoted MeOH-treated) or with 100 mM ammonia. There are small line shape differences in the untreated vs MeOH-treated line shapes, but for our purposes the major difference is an increase in the multiline intensity at the expense of the $g = 4.1$ signal induced by the addition of methanol.[47] The ammonia treatment gives a more dramatic alteration in the EPR spectrum. Figure 5 compares the CW-EPR spectra (bold lines) of MeOH and ammonia-treated spinach PS II centers. The addition of the ammonia leads to an increase in the number of observed lines in the CW spectrum as well as a decrease in the hyperfine splitting of these lines. This decrease in the observed splitting suggests that the average effective $^{55}Mn$ hyperfine coupling in ammonia-treated PS II centers is smaller than the average effective $^{55}Mn$ hyperfine coupling in MeOH-treated PS II centers.

It is important that we demonstrate that the light-minus-dark $S_2$-state spectrum measured with ESE spectroscopy corresponds to the spectrum obtained with conventional CW-EPR detection. Figure 6A shows the light-dark ESE-EPR field swept spectrum of MeOH-treated PS II centers acquired using $\pi/2$ microwave pulses of 100 ns width. Figure 6B compares the first derivative of the spectrum in Figure 6A with the CW-EPR spectrum of MeOH-treated PS II centers in Figure 5. Given the similarity of the two traces in Figure 6B, we can conclude that the ESE-EPR and CW-EPR experiments are probing the same paramagnetic system. In prior reports from our laboratory, we reported the ESE-EPR field swept spectra of PS II centers using $\pi/2$ microwave pulses of 15 ns width. Such short microwave pulses create coherences between the spin states of magnetic nuclei coupled to electron spin. These are the very coherences that give rise to the ESEEM effect, and this well-characterized effect causes the line shape of the ESE-EPR spectrum to depend on the choice of $\tau$ used in the EPR pulse sequence.[48] As a result, our previously reported ESE-EPR spectra of PS II centers are slightly distorted with respect to the longer pulse data of Figure 6A or the CW-EPR spectra. For example, Figure 6C compares the 15 ns pulse width ESE-EPR field swept spectra of MeOH-treated PS II centers at a number of different values of $\tau$. (Trace b of Figure 6C is similar to the field swept spectra reported previously.[5,16]) Åhrling et al.[20] have recently raised the concern that the asymmetry of the line shape of trace b of Figure 6C is evidence that two different species are responsible for the ESE-ENDOR data in our previous reports.[5,16,40] However, it is clear from the $\tau$-dependence of Figure 6C that the line shape of trace b results simply from our use of short microwave pulses and not from the presence of a second paramagnetic species.

Figure 7 shows the "raw" illuminated $S_2$ and dark adapted $S_1$ ENDOR spectra from MeOH-treated, untreated, and ammonia-treated PSII membranes. It is clear from the "raw" spectra that the $S_1$ baseline spectra are rather flat, with very small features as compared to the $S_2$ spectra. Some of these remnant features may be due to small amounts of $S_2$-state multiline remaining after the annealing step (for example, trace C), while we may have a small amount of Mn(II) $^{55}Mn$ ENDOR

(47) Zimmerman, J. L.; Rutherford, A. W. *Biochemistry* **1986**, *25*, 4609−4615.

(48) Schweiger, A. *Angew. Chemie.* **1991**, *30*, 265−292.

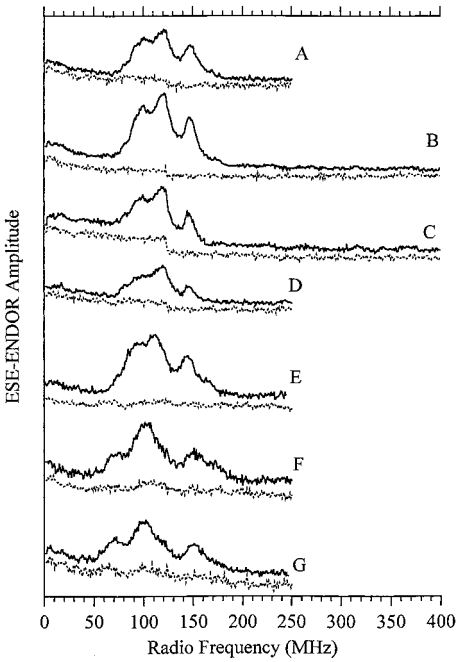


**Figure 7.** (A−D) ESE-ENDOR spectra of 3% MeOH-treated spinach PS II centers trapped in the $S_1$-state (dashed line) and $S_2$-state (solid line); (E) ESE-ENDOR spectrum of untreated spinach PS II centers trapped in the $S_1$-state (dashed line) and $S_2$-state (solid line); (F and G) ESE-ENDOR spectra of 100 mM $NH_4Cl$-treated spinach PS II centers trapped in the $S_1$-state (dashed line) and $S_2$-state (solid line). Experimental conditions: magnetic field = (A) 3950 G; (B) 3780 G; (C) 3500 G; (D) 3300 G; (E) 3767 G; (F) 3720 G; (G) 3450 G; microwave frequency = (A−D) 10.185 GHz; (E) 10.151 GHz (F and G) 10.2045 GHz; $\pi/2$ microwave pulse length = 15 ns; $\tau$ = 195 ns; $T$ = 40 $\mu$s; radio frequency pulselength = 38 $\mu$s; microwave power = 30 W; radio frequency power = 100 W; repetition time = 2 ms; temperature = 4.24 K.

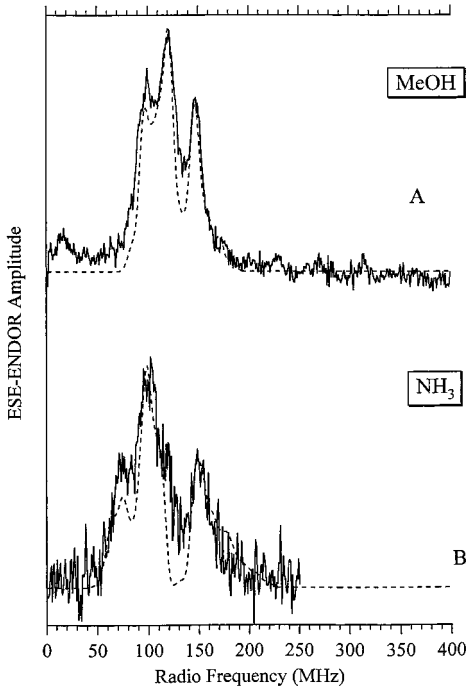


**Figure 8.** $S_2-S_1$ ESE-ENDOR difference spectra of (A) 3% MeOH-treated spinach PS II centers at 3780 G (solid line) and spectral simulation (dashed line); (B) 100 mM $NH_4Cl$-treated spinach PS II centers at 3450 G (solid line) and spectral simulation (dashed line).

contamination (most notably the ammonia-treated samples of traces F and G). Regardless of origin, the "dark" background ENDOR features are relatively small, and the baselines are relatively flat (especially considering the enormous frequency ranges swept, up to 400 MHz) This lack of features, along with the ESE-EPR data of Figure 6, gives us a high degree of confidence in analyzing the subsequent light-minus-dark ENDOR data as arising from the $S_2$ multiline signal. We also note there are no features beyond approximately 175 MHz in the illuminated spectra that arise above the noise level of the background spectra.

Figure 7A−D compares the ESE-ENDOR spectra of MeOH-treated PS II centers in the $S_1$ (dashed) and $S_2$ (solid) states at four different magnetic field positions. These spectra compare quite nicely to those that we have previously published.[5,16,40] Figure 7E displays the ESE-ENDOR spectra of untreated PS II centers at single magnetic field. It is clear that the treatment of PS II centers with MeOH does not result in major changes in the ESE-ENDOR spectrum from the untreated ESE-ENDOR spectrum, consistent with the rather similar CW-EPR line shapes. Figure 7F,G show the ESE-ENDOR spectra of ammonia-treated PS II centers at two different magnetic fields. The binding of ammonia results in a dramatic change in the ESE-ENDOR spectrum with respect to the untreated and MeOH-treated spectra.

Figure 8 displays the actual light-minus-dark $^{55}$Mn ENDOR spectra. Figure 8A (bold line) shows the $S_2-S_1$ MeOH PS II difference ENDOR spectrum generated from traces B of Figure 7, and Figure 8B (bold line) shows the $S_2-S_1$ ammonia-treated PS II difference ENDOR spectrum generated from traces G of Figure 7. We assign the intense features between 65 and 175 MHz to the $^{55}$Mn nuclear transitions of the manganese ions of the OEC. For MeOH PS II centers, distinct strong peaks are observed at 100, 120, and 148 MHz. For ammonia PS II centers, distinct strong peaks are observed at 75, 102, and 150 MHz. The difference spectra of the ammonia-treated sample has somewhat worse signal-to-noise because the 30 s annealing step needed to permit ammonia binding results in some loss of the $S_2$-state. A small peak in the MeOH sample difference spectrum at 15 MHz is easily assignable to protons. We have performed ESE-ENDOR experiments on multiple independently prepared PS II samples and observe no reproducible features at frequencies above 175 MHz, whereas the features in the 65 to 175 MHz range are very reproducible. We conclude that any weak features beyond 175 MHz are simply low frequency noise that has not been completely suppressed by averaging. We therefore assert that there is no spectroscopic evidence for $^{55}$Mn transitions at frequencies above 175 MHz in the $S_2$-state.

Additionally, Figures 7 and 8 clearly show that the $^{55}$Mn transition frequencies are altered upon binding of ammonia to the manganese cluster, in a manner perfectly consistent with the changes in the CW-EPR spectra shown in Figure 5. In the limit where the hyperfine coupling is larger than the Larmor frequency of a nucleus (3.7 MHz for $^{55}$Mn at 3780 G), the ENDOR spectrum is centered at roughly $A_{iso}/2$. With this association in mind, it is quite clear from Figure 8 that the average $^{55}$Mn hyperfine coupling is smaller in the ammonia-treated PS II centers than in the MeOH-treated PS II centers, as was predicted from the CW-EPR spectra in Figure 5. This correlation between the changes in the CW-EPR and ESE-ENDOR spectra upon binding of ammonia provides a further indication that the ESE-ENDOR spectra in Figures 7 and 8 arise from the same $S_2$-states of the manganese cluster of the OEC that give rise to the multiline CW-EPR signals and not from some mysterious other alternative paramagnetic species.[20]

**Table 4.** Parameters Used to Simulate the $S_2$-State Multiline CW-EPR and ESE-ENDOR Spectra in Figures 5 and 8

| | MeOH | | | | ammonia | | | |
|---|---|---|---|---|---|---|---|---|
| | $Mn_A$ | $Mn_B$ | $Mn_C$ | $Mn_D$ | $Mn_A$ | $Mn_B$ | $Mn_C$ | $Mn_D$ |
| $A'_X$ (MHz) | −232 | 200 | −311 | 180 | 208 | −150 | 222 | −295 |
| $A'_Y$ (MHz) | −232 | 200 | −311 | 180 | 208 | −150 | 222 | −315 |
| $A'_Z$ (MHz) | −270 | 250 | −270 | 240 | 158 | −112 | 172 | −390 |
| $P'_{\|}$ (MHz) | −3 | −3 | 8 | 1 | −3 | −3 | 1 | 8 |
| $\eta$ | 0.1 | 0.1 | 0.1 | 0.1 | 0.1 | 0.1 | 0.1 | 0.1 |
| $A'_{iso}$ (MHz) | −245 | 217 | −297 | 200 | 191 | −137 | 205 | −333 |
| $A'_{dip}$ (MHz) | −13 | 17 | 14 | 20 | −17 | 13 | −17 | −28 |
| $g'_X$ | 1.97 | | | | 1.99 | | | |
| $g'_Y$ | 1.97 | | | | 1.99 | | | |
| $g'_Z$ | 1.99 | | | | 1.96 | | | |
| oxidation state | IV | IV | III | IV | IV | IV | IV | III |

**Spectral Simulations.** We have simultaneously simulated the CW-EPR and ESE-ENDOR data of MeOH-treated PS II and ammonia-treated PS II centers using the spin Hamiltonian given by eq 2. The results of both sets of simulations are shown with dashed lines in Figure 5 (CW-EPR) and Figure 8 (ESE-ENDOR), and the resulting simulation parameters are given in Table 4. To simulate the strong ESE-ENDOR features between 65 and 175 MHz, the complete lack of ESE-ENDOR features above 175 MHz and the CW-EPR spectra of the MeOH and ammonia-treated PS II data, we require four effective $^{55}$Mn hyperfine tensors. Examination of Table 4 shows that the average isotropic hyperfine coupling drops from 240 MHz (86 G) for the MeOH-treated sample to 216 MHz (77 G) for the ammonia-treated sample. This correlates with the change in the respective CW-EPR spectra in Figure 5, where the average splitting of the hyperfine lines is reduced from 252 MHz (90 G) for the MeOH-treated sample to 228 MHz (82 G) for the ammonia-treated sample.

For completeness, it is necessary to consider the possibility that the $S_2$-state EPR signals do not arise from the coupling of four $I = {}^5/_2$ $^{55}$Mn nuclei to an $S_T = {}^1/_2$ electron spin system but instead arise from two or three $^{55}$Mn nuclei. We discussed this issue in our original report of the ESE-ENDOR spectrum of the $S_2$-state and concluded that four $^{55}$Mn hyperfine tensors are required for proper simulation.[40] However, dinuclear models for the $S_2$-state of the manganese cluster are still being proposed.[20] While it is possible to use just two or three $^{55}$Mn hyperfine tensors to generate simulated ENDOR spectra containing features between 100 and 150 MHz, the effective $^{55}$Mn hyperfine tensors cannot have components above ≈320 MHz. The lack of high frequency hyperfine components results in simulated CW-EPR spectra using two or three manganese couplings that are significantly narrower than the experimental spectra. Conversely, it is possible to use two or three $^{55}$Mn nuclei hyperfine tensors to obtain a CW-EPR spectrum that resembles the $g = 2$ multiline signal. However, at least one of these hyperfine tensors must have components greater than ≈350 MHz, and a component of this magnitude would lead to ENDOR transitions at frequencies greater than 175 MHz, which we do not observe in our data. Furthermore, to fully reproduce the CW-EPR spectra of the $g = 2$ multiline CW-EPR spectrum using only two or three $^{55}$Mn nuclei, it is necessary to include very large $^{55}$Mn nuclear quadrupole tensors in the simulations. This requirement is clearly shown by Åhrling et al.,[20,21] who assume that two $^{55}$Mn nuclei are responsible for the $S_2$-state multiline signal and use very large $^{55}$Mn quadrupole tensors (on the order of $P = 50-80$ MHz) that have no experimental precedence in the model compound literature. In our simulations using four nuclei, we are able to use precedented values for the $^{55}$Mn quadrupole tensors, ($P < 10$ MHz). Because we are unable to simultaneously simulate the CW-EPR and ESE-ENDOR data using two or three hyperfine tensors, we assign the nuclearity of the manganese cluster to four manganese ions. As a result, we do not consider dinuclear or trinuclear models for the $S_2$-state manganese cluster to be viable.

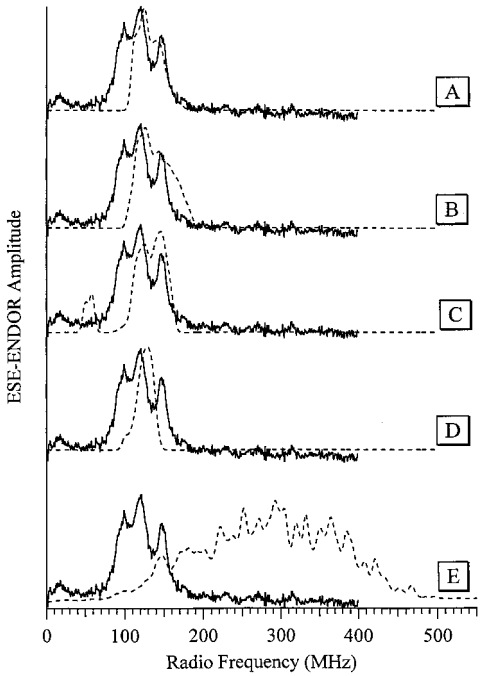


**Figure 9.** Comparison of ESE-ENDOR spectrum of 3% MeOH-treated spinach PS II centers (solid line) with spectral simulations using parameters listed in Table 1 (dashed lined). (A and B) Zheng and Dismukes;[17] (C) Hasegawa et al.;[18,19] (D) Lakshmi et al.;[49] (E) Åhrling et al.[20,21]

## Discussion

**Comparison with Previous Simulations.** As mentioned above and shown in Table 1, a number of researchers have reported simulations of the $S_2$-state CW-EPR multiline spectrum using quite varied simulation parameters. Figure 9 compares the ESE-ENDOR spectrum of MeOH-treated PS II centers with the simulations using the various parameters listed in Table 1. It is clear from this comparison that none of the effective $^{55}$Mn hyperfine tensors derived from previous simulations of the CW-EPR data matches our experimental ESE-ENDOR data. Figure 9 and its comparison with our own simulations in Figures 5 and 8 very dramatically demonstrate the power of being able to perform simultaneous simulations of the CW-EPR and ESE-ENDOR data. While the models of Hasegawa et al.[18,19] as well as those of Zheng and Dismukes[17] do reproduce the high-frequency portion of the ESE-ENDOR data, they both fail to reproduce the low-frequency side. The parameters of Lakshmi et al.[49] appear to result in an average of the ESE-ENDOR spectrum.

The comparison in Figure 9 is slightly prejudicial in that the $^{55}$Mn nuclear transition frequencies in an ENDOR spectrum are sensitive to the exact value of the $^{55}$Mn nuclear quadrupole tensor, $P$, in eq 2, whereas the electron spin transition frequencies in a CW-EPR spectrum are not normally very sensitive to small to moderate values the $^{55}$Mn quadrupole parameters. The possibility exists then that the CW-EPR derived effective $^{55}$Mn hyperfine tensors proposed by Hasegawa et al.,[18,19] Zheng and

(49) Lakshmi, K. V.; Eaton, S. S.; Eaton, G. R.; Brudvig, G. W. *Biochemistry* **1999**, *38*, 12758−12767.

Dismukes,[17] and Lakshmi et al.[49] can be made to reproduce our ENDOR data with the inclusion of $^{55}$Mn quadrupole parameters. However, we have used values of $P$ as large as ± 15 MHz and have not been able to reconcile the CW-EPR derived tensors of these three researchers with our ENDOR data.

The spectral analysis of the Åhrling et al.[20,21] dinuclear models already contains a set of proposed $^{55}$Mn quadrupole terms, and as a result the comparison of the experimental ENDOR spectrum with the calculated ENDOR spectrum based on their proposed parameters is completely fair and rigorous. It is clear from Figures 7 and 8 that no features at frequencies greater than 200 MHz can be reliably assigned to an ENDOR transition. However, the dinuclear calculated spectrum (Figure 9E) predicts that the majority of the ESE-ENDOR spectrum results from $^{55}$Mn nuclear spin transitions with frequencies greater than 200 MHz. It is clear from our ESE-ENDOR spectra of the dinuclear manganese systems[16,34,38] and in Figure 3 that we are capable of observing broad signals at frequencies approaching and greater than 200 MHz. Moreover, the dinuclear cluster parameters fail to reproduce the strong features that we do observe below 175 MHz. As a result, we feel that our ESE-ENDOR data provide compelling direct experimental evidence against the dinuclear model of Åhrling et al.[20,21]

**Structural Analysis.** At this point in the analysis we have accurately determined hyperfine tensors (Table 4) in the coupled representation (eq 2). To test possible structural models, it is necessary to calculate the intrinsic hyperfine coupling (those of eq 1) for each Mn(III) and Mn(IV) ion incorporated into the structural model. This requires calculating the respective projection matrices, in direct analogy to our analysis of the dinuclear clusters. If these calculated intrinsic tensors are consistent with the "standard" range of the Mn(III) or Mn(IV) tensor components listed in Table 2 then we consider the structural model used to generate the projection factors to be viable as far as EPR/ENDOR spectroscopy is concerned. Spectral simulation is straightforward for a Mn(III,IV) dinuclear structure since there is only one Mn−Mn isotropic exchange pathway and only one permutation of the Mn(III) and Mn(IV) ions. In a tetranuclear manganese cluster, six Mn−Mn isotropic exchange pathways exist. Additionally, for a given set of isotropic exchange couplings, the various permutations of the $S = 2$ Mn(III) and $S = {}^3/_2$ Mn(IV) ions among the four sites result in different sets of projection factors. Also, as discussed for the dinuclear case, it is important to take into account the zero-field-splitting tensors of the Mn(III) and Mn(IV) ions.[40,41]

Our approach is to incorporate structural constraints from EXAFS and XANES experiments into our magnetic model and to use zero-field-splitting and isotropic exchange coupling parameters with model compound literature precedents. "Successful" models will meet these X-ray spectroscopy and model compound parameter constraints as well as the EPR/ENDOR established $^{55}$Mn hyperfine and quadrupole tensor constraints derived from our simulations of the data in Figures 5 and 8. Additionally, a structural model proposed and successfully tested for, say, the MeOH-treated $S_2$-state, should also be able to account for data from other magnetic states, such as the ammonia-altered multiline EPR/ENDOR data, the $g = 4.1$ EPR data, and the EPR spectra, with chemically reasonable assumptions for structural changes that lead to the altered magnetic and electronic properties. Only if we fail at these steps will we turn to models that conflict with the X-ray or established model chemistry data: for example, assuming strong ferromagnetic couplings within 2.7 Å dinuclear cores, using a Mn(III,III,III,IV) valence assignment for the $S_2$-state, or assuming hyperfine or quadrupolar tensor components that differ dramatically from literature values for biological or model compound Mn(III) and Mn(IV) ions.

We begin by discussing the constraints we build into our model selection procedure: We use the XANES $S_2$-state assignment of one $S = 2$ Mn(III) ion and three $S = {}^3/_2$ Mn(IV) ions.[11,13,15] Extended X-ray absorption fine structure (EXAFS) spectroscopy predicts the existence of three distinct Mn−Mn distances, two 2.7 Å distances, and one 3.3 Å distance.[11,12,15] Figure 1 shows a number of tetranuclear structures consistent with these distance constraints. Structures 1−4 collectively represent a "dimer of dimers" motif, in which two di-$\mu$-oxo bridged Mn "dimers" (Mn−Mn distance 2.7 Å) are linked together with the longer 3.3 Å bridging distance. Structures 5−7 collectively represent a trimer−monomer motif, in which two di-$\mu$-oxo bridged Mn dimers (Mn−Mn distance 2.7 Å) share a common Mn ion and are linked to the fourth Mn ion with the longer 3.3 Å distance. Structures 8 and 9 represent two unrelated motifs with every Mn ion 2.7 Å away from at least two other manganese ions and 3.3 Å from at least one manganese ion. Structure 10 can be considered to be related to the "dimer of dimers" motifs (structures 1−4).

In terms of isotropic exchange interactions, the 2.7 Å $\mu$-oxo bridged structure gives rise to a strong antiferromagnetic coupling, $J < -100$ cm$^{-1}$.[16,34,42,50,51] On the other hand, the longer 3.3 Å distance can be associated with weaker antiferromagnetic or ferromagnetic couplings, $-30 < J < 20$ cm$^{-1}$.[41,50] While exceptions to these accepted ranges can be found or postulated,[17] it is our protocol to construct a model using the best characterized, nonexceptional parameters. The zero-field-splitting of Mn(III) ions should be $|D_{III}| = 1-4$ cm$^{-1}$. As we did for the analysis of the dinuclear complexes, we assume $|D_{IV}| = 0$ cm$^{-1}$ for the Mn(IV) ions. The ligand environment around the Mn ions should be sufficiently symmetric to support the small values of $^{55}$Mn quadrupole tensors, $P$, in Table 4. Finally, a number of electron paramagnetic resonance experiments have demonstrated that the $S_2$-state multiline signal arises from a ground spin state and that the next excited spin state is approximately 30 to 40 cm$^{-1}$ higher in energy.[1,44−46]

Our initial constraints are therefore (i) oxidation states: three $S = {}^3/_2$ Mn(IV) ions and one $S = 2$ Mn(III); (ii) zero-field-splitting: for Mn(III) $|D_{III}| = 1-4$ cm$^{-1}$; for Mn(IV) $D_{IV} = 0$ cm$^{-1}$; (iii) exchange coupling: 2.7 Å distance, strong antiferromagnetic coupling $J < -100$ cm$^{-1}$; 3.3 Å distance, weak antiferro- or ferromagnetic coupling $-30 < J < 20$ cm$^{-1}$; (iv) first excited spin state: calculated to be 30 cm$^{-1}$ above ground state.

**"Dimer of Dimers" Model.** The most discussed structural model for the manganese cluster has been the "dimer of dimers" model, structure 1 in Figure 1. One dimer consists of a Mn(III)−Mn(IV) unit and the other dimer consists of a Mn(IV)−Mn(IV) unit. However, it is straightforward to demonstrate that these two structures do not satisfy condition 4. Because the Mn(IV)−Mn(IV) unit will have an effective spin $S = 0$, the magnetic properties of the tetranuclear cluster will be determined by the exchange coupling of the Mn(III)−Mn(IV) dimer. As a consequence, the first excited state of the system will be determined by the magnitude of the exchange coupling for the Mn(III)−Mn(IV) unit, $J_{III,IV} \approx -100$ to $-150$ cm$^{-1}$. This system will then have a first excited state 300−450 cm$^{-1}$ above the ground state, which violates condition 4. The other three "dimer

(50) Manchanda, R.; Brudvig, G. W.; Crabtree, R. H. *Coord. Chem. Rev.* **1995**, *144*, 1−38.
(51) Law, N. A.; Kampf, J. W.; Pecoraro, V. L. *Inorg. Chim. Acta* **2000**, *297*, 252−264.

**Scheme 1**

(5)

$C$ ⋮ $A \cdots B$ ⋱ $D$

$J_{AB} \leq -100\ cm^{-1}$

$J_{BC} \leq -100\ cm^{-1}$

$+20\ cm^{-1} \geq J_{BD} > 15\ cm^{-1}$

$J_{AC} = J_{AD} = J_{CD} = 0\ cm^{-1}$

(6)

$A$ ⋮ $B \cdots C$ ⋱ $D$

$J_{AB} \leq -100\ cm^{-1}$

$J_{BC} \leq -100\ cm^{-1}$

$-20\ cm^{-1} \leq J_{CD} < -15\ cm^{-1}$

$J_{AC} = J_{AD} = J_{BD} = 0\ cm^{-1}$

of dimers" structures, 2−4, also will not have excited states that satisfy condition 4. Moreover, with the strongly exchange-coupled dimers only weakly coupled through one (structures 1−3) or two (structure 4) longer bridges, we have difficulty getting sufficiently large projection matrices on the two Mn nuclei of the nonmixed valence, $S = 0$ "silent" dimer. The couplings are rigorously zero in the symmetrically coupled case with four equivalent interdimer $J$ couplings.[17] However, a lower symmetry coupling, for example, a single antiferromagnetic interaction between one end of each dimer (structure 1 of Figure 1) introduces nonzero projection matrices onto the "silent" dimer. Still, unless we make the cross dimer couplings stronger and/or the intradimer couplings weaker than our condition 3 constraints, the projection matrices for the "silent" dimer are too small to match the experimental EPR/ENDOR results. These couplings could be outside the range of our condition 3 constraints taken from the model literature. However, our favored structures (5−7) (vide infra) work beautifully within the precedented constraints, and therefore, we strongly favor these.

Structures 8, 9, and 10 consist of multiple dinuclear Mn units. Structure 10 will not satisfy condition 4. If each of the dinuclear units in structures 8 and 9 have similar isotropic exchange couplings then the ground spin state for the two structures will not be $S = {}^1/_2$. To make the ground spin state $S = {}^1/_2$, the magnetic coupling of at least one of the dinuclear units must be made weaker than the magnetic coupling of the other dinuclear units. The weaker coupling ($J = -10$ to $-20\ cm^{-1}$ needed to satisfy condition 4 will essentially convert structures 8 and 9 into structures that are magnetically equivalent to our favored structures 5−7, the trimer−monomer structures

**Trimer/Monomer Model.** As argued above, with our initial set of constraints used in selecting structural models, structures 1−4 and 8−10 do not suffice. Again, if we did not have possible structures that did pass the test of these constraints, we would have to go back and loosen some of these assumptions. Fortunately, the class of structures with a strongly antiferromagnetically coupled trimer core, weakly coupled to a fourth "dangling" manganese (structures 5−7), work quite well; we therefore favor this class of structures for the $S_2$-state of the OEC. Moreover, as we discuss later, these structures allow for reasonable chemical triggers for the formation of the ammonia-altered multiline and $g = 4.1$ $S_2$ forms, as well as a successful basis for modeling what is known of the $S_0$-state magnetics. Scheme 1 shows the simplest set of exchange couplings for structures 5 and 6 of Figure 1 that satisfy our assumptions stated above. In this scheme, Mn ions A, B, and C form a strongly coupled trinuclear core while Mn D is weakly coupled to the core. The coupling scheme for structure 7 can be generated from the appropriate coupling scheme of structure 5 or 6 simply by making $J_{AC} \neq 0$. As long as $J_{AC}$ is ferromagnetic or antiferromagnetic with $0 < |J_{AC}| < |J_{AB}|/2$ and $|J_{BC}|/2$ then the ground spin state will be 1/2. Because $Mn_D$ is only weakly coupled to the core, we refer to this as the "dangling" manganese. For simplicity, we will focus on structure 6 for the purpose of discussion; however, all of our conclusions apply to any structure that can be made to assume the exchange coupling schemes in Scheme 1. Figure 10 shows a molecular model of the manganese cluster and the OEC based on structure 6. Figure 11 shows the four possible arrangements of the Mn(III) and Mn(IV) ions for the structure given in Figure 10.

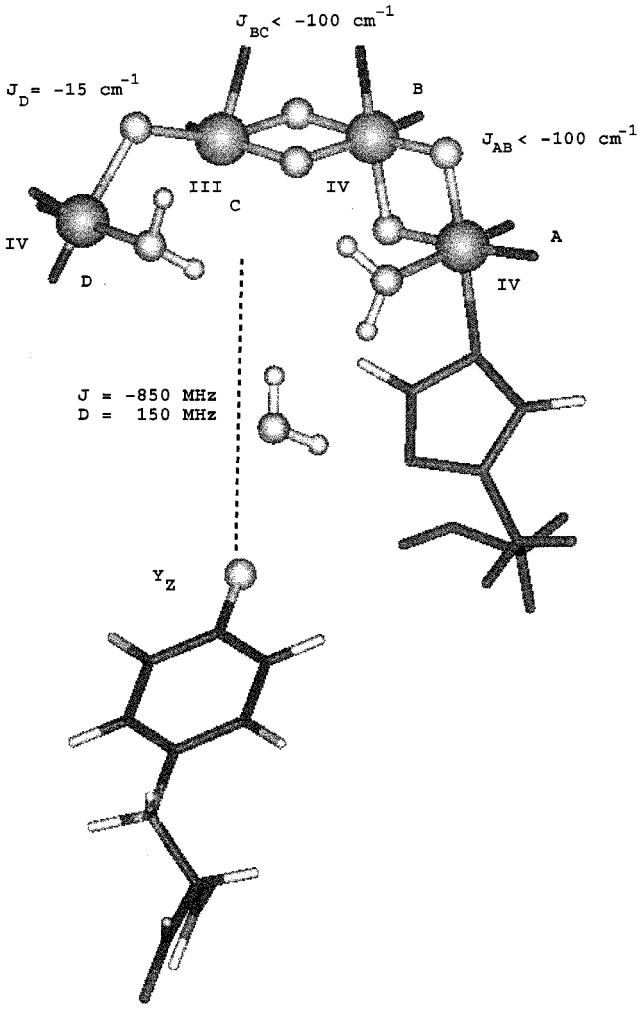


**Figure 10.** A preferred structure of the oxygen evolving complex of PS II in the $S_2$-state of MeOH-treated PS II centers.

With the possible structures of the manganese complex narrowed to one archetypical structure, it is now possible to use the effective $^{55}Mn$ hyperfine tensors for the MeOH and ammonia PS II centers in Table 4 to determine the exchange couplings and zero-field-splitting terms of the manganese cluster through the calculation of projection matrices that transform the effective $^{55}Mn$ hyperfine tensors in Table 4 into the "standard" intrinsic tensors in Table 2. Unlike the dinuclear case, no simple general analytical equation for the projection factors exists for a general low-symmetry tetranuclear cluster. However, the projection factors can be calculated numerically as shown by Gatteschi and Bencini.[31] Table 5 shows the calculated projection factors for the three possible arrangements of the Mn(III) ion in structure 6. At this point in the analysis, we are neglecting the effects of the Mn(III) zero-field-splittings, and therefore the projection factors are isotropic (vide infra).

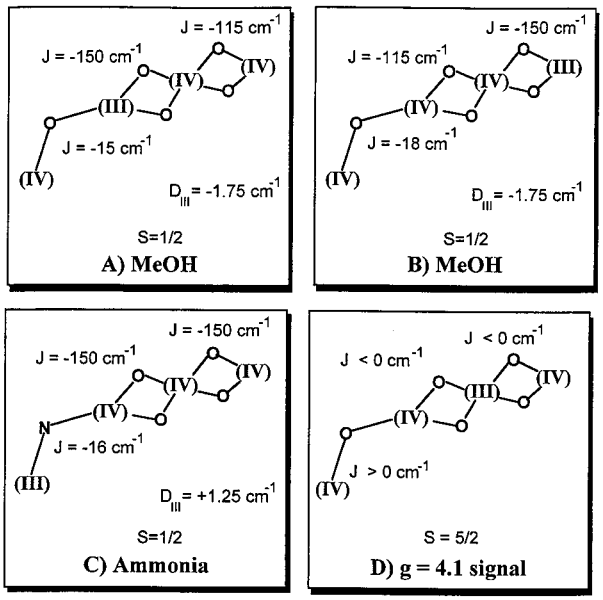


**Figure 11.** Arrangements of oxidation states predicted by the "dangler" model for the manganese cluster. (A and B) MeOH-treated PS II centers trappedin the $g = 2$ multiline form; (C) ammonia-treated PS II centers trapped in the $g = 2$ multiline form; (D) PS II centers trapped in the $g = 4.1$ form.

**Table 5.** Sample Projection Matrices for Permutations of Oxidation States within Our Trinuclear/Monomer Structure

| $J_{AB} = J_{BC} = -150$ cm$^{-1}$ and $J_{CD} = -15$ cm$^{-1}$ | | | | |
|---|---|---|---|---|
| Mn ion | [IV IV III]IV | [III IV IV]IV | [IV III IV]IV | [IV IV IV]III |
| A | 1.34 | 1.77 | −0.70 | −0.80 |
| B | −1.00 | −1.00 | 0.76 | 0.65 |
| C | 1.66 | 1.23 | −0.73 | −0.84 |
| D | −1.00 | −1.00 | 1.66 | 2.00 |

Approximately the same projection factors are obtained for structures 5−7. In our calculations of projection factors, we find that there is no practical methodology to distinguish between structures 5−7 using EPR data alone. This inability to distinguish between the different structures arises simply from the spread commonly assumed for the standard hyperfine tensors shown in Table 2.[16,17,40−42] In a recent report, Hasegawa et al.,[19] using modeling constraints similar to ours, also conclude that the structure of the manganese cluster consists of a core of three manganese ions and a fourth loosely coupled manganese ion. However, they propose that structures 5 and 6 are not appropriate structural models for the manganese cluster and propose a very specific version of structure 7, referred to as a distorted cubane motif,[19] where $J_{BC}$ and $J_{AC}$ are very similar in energy ($0 > \approx J_{BC} > 0.5\ J_{AB} \approx -120$ cm$^{-1}$).[52] This coupling scheme is required because it is the only manner in which they were able to generate a projection factor small enough to support the 100-MHz hyperfine tensor for $Mn_C$ in Table 2 while still maintaining the needed 2.7 Å distances required by the EXAFS data. However, we show in Figure 9 that the proposed $^{55}$Mn hyperfine tensors of Hasegawa et al. are not consistent with our ESE-ENDOR data. While these authors claim that their $^{55}$Mn tensors reproduce our experimental ENDOR data, they do not report the calculated ESE-ENDOR spectrum. Until Hasegawa et al. can reconcile their effective $^{55}$Mn hyperfine tensors with our experimental ENDOR data, we feel there is no experimental justification to exclude structures 5 and 6.

(52) Although Hasegawa et al. initially based this motif on a trimer/monomer topology, their structural model is better described as a monomer/dimer/monomer topology from the perspective of the exchange couplings they use.

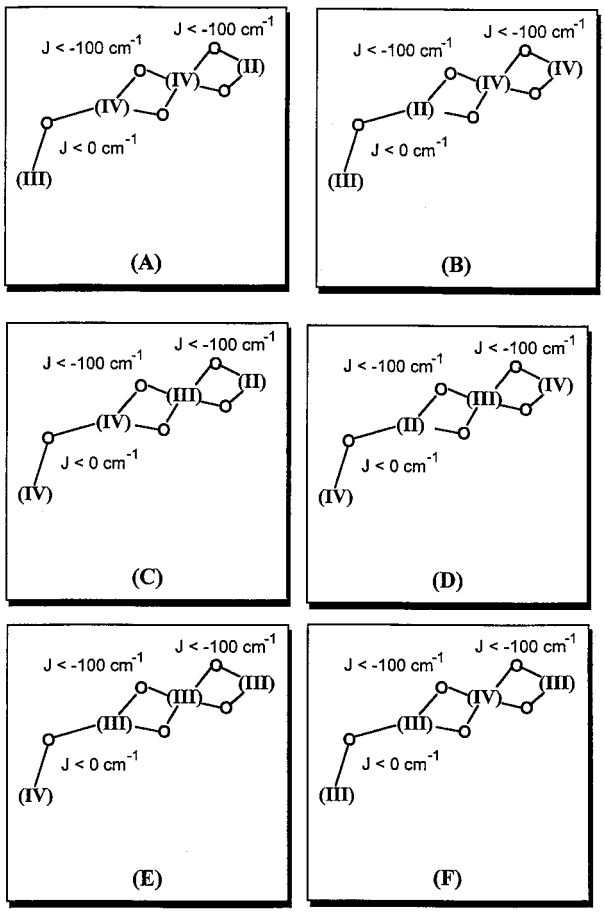


**Figure 12.** Possible arrangements of oxidation states predicted by the "dangler" model for the manganese cluster in the $S_0$-state for the Mn(II,III,IV,IV) and Mn(III,III,III,IV) valence assignments.

In Figure 10, and subsequent Figures 11 and 12, we have chosen a structure based on Figure 1 (structure 6), the linear trimer−monomer model. Our analysis is based on the topology of couplings, and the model does not have to be rigorously linear as shown in Figure 1. We have chosen to display it in a bent cis geometry, which maintains an overall shape similar to the Berkeley "dimer of dimers" structure. Structure 6, in which the "dangling" Mn is located off one end of the trimer core, offers the advantage that it distributes $\mu$-oxo bridging ligands more evenly than the center-located dangler model (structure 5), which loads five $\mu$-oxo bridges onto the central Mn of the trimer. In subsequent analysis, we will focus on the linear trimer−monomer structure, but we again note that analogous arguments can be made for the alternate trimer−monomer structures.

As shown in Table 4, the isotropic portion of three of the hyperfine tensors for the MeOH-treated PS II sample are all very close to the standard isotropic hyperfine tensors for a Mn(IV) ion. This pattern suggests all three Mn(IV) projection matrices are close to 1. Columns 1 and 2 of Table 5 have just such a pattern. In this case, the Mn(III) ion is located on one of the ends of the trinuclear core, $Mn_A$ or $Mn_C$, as shown in Figure 11A,B.

Before the projection factors in Table 5 can be used to calculate the intrinsic $^{55}$Mn hyperfine tensors of the manganese ions, it is necessary to take into account the effect of the zero-field-splitting term of the Mn(III) ion. Plots of intrinsic hyperfine values vs $D$ similar to those in Figure 4 indicate that the zero-

**Table 6.** Calculated Projection Matrices and Intrinsic $^{55}$Mn Hyperfine Tensors for 3% MeOH-Treated PS II Centers

$J_{AB} = -115$ cm$^{-1}$, $J_{BC} = -150$ cm$^{-1}$ and $J_{CD} = -15$ cm$^{-1}$, $D_{III} = -1.75$ cm$^{-1}$

| | projection factors | | intrinsic hyperfine (MHz) | |
|---|---|---|---|---|
| ion | ⊥ | ∥ | $A_{iso}$ | $A_{dip}$ |
| $Mn_A$(IV) | 1.22 | 1.38 | −192 | −2.0 |
| $Mn_B$(IV) | −0.95 | −1.10 | −216 | −5.3 |
| $Mn_C$(III) | 1.62 | 1.87 | −175 | 15.6 |
| $Mn_D$(IV) | −0.90 | −1.17 | −202 | 0.0 |

**Table 7.** Calculated Projection Matrices and Intrinsic $^{55}$Mn Hyperfine Tensors for Ammonia-Treated PS II Centers

$J_{AB} = -150$ cm$^{-1}$, $J_{BC} = -150$ cm$^{-1}$ and $J_{CD} = -16$, $D_{III} = 1.25$ cm$^{-1}$

| | projection factors | | intrinsic hyperfine (MHz) | |
|---|---|---|---|---|
| ion | ⊥ | ∥ | $A_{iso}$ | $A_{dip}$ |
| $Mn_A$(IV) | −0.89 | −0.65 | −237 | −3.6 |
| $Mn_B$(IV) | 0.71 | 0.53 | −211 | −0.2 |
| $Mn_C$(IV) | −0.92 | −0.69 | −245 | −3.0 |
| $Mn_D$(III) | 2.09 | 1.81 | −166 | −23.0 |

field-splitting term for the Mn(III) ion is $D = -1.25$ to $-2.25$ cm$^{-1}$ (data not shown). Table 6 shows the results of using the projection factors for the case $D = -1.75$ cm$^{-1}$, $J_{CD} = -15$ cm, and the structure of Figure 11A to calculate the intrinsic $^{55}$Mn hyperfine tensors of the manganese cluster. The calculated intrinsic hyperfine tensors are all slightly lower than the average Mn(III) and Mn(IV) tensors in Table 2, but they are well within the prescribed range of the standard tensors in Table 2.

Although we predict a fairly large range for the possible values of $D_{III}$, its inclusion in our calculation of the projection factors is absolutely required. The first excited spin state of the multiline form of the manganese cluster is ≈30 cm$^{-1}$ above the ground state[1,21,44−46] and even a $D_{III}$ as small as 0.5 cm$^{-1}$ will affect the projection matrices. However, the previous studies of Zheng and Dismukes[17] and Hasegawa et al.[18,19] did not include $D_{III}$. The inclusion of $D_{III}$ is of particular importance for the analysis of Zheng and Dismukes since they propose that the valences of the manganese cluster are Mn(III,III,III,IV). For the Mn(III,IV,IV,IV) assignment we are using, without the inclusion of $D_{III}$ our effective $^{55}$Mn hyperfine tensors predict Mn(IV) intrinsic hyperfine tensors with larger dipolar couplings than expected from model compounds and Mn catalase. If we had not included the effect of $D_{III}$ in our analysis, these larger couplings would have led us into favoring Mn(III) assignments over the Mn(IV) assignments, in that Mn(III) ions are expected to have intrinsically larger dipolar couplings than Mn(IV) ions.

**Ammonia Structural Analysis.** A similar analysis can be made for the ammonia-treated PS II sample. Examination of Table 4 for the ammonia-treated PS II sample shows that three of the tensors for the ammonia parameters have isotropic components smaller than the standard Mn(IV) isotropic value in Table 2. Examination of Table 5 is suggestive that the valence assignment Mn(IV,IV,IV,III) (column 4) is the appropriate set of projection factors for the manganese cluster in the ammonia PS II sample. Plots of the calculated intrinsic hyperfine tensors vs $D$ indicate that the zero-field-splitting term for the Mn(III) ion is $D = 0.75-1.75$ cm$^{-1}$ (data not shown). Table 7 shows the projection factors for the Mn(IV,IV,IV,III) valence assignment calculated with $D = +1.25$ cm$^{-1}$ and $J_{CD} = -16$ cm$^{-1}$. Again, the calculated intrinsic hyperfine tensors are consistent with the standard tensors in Table 2. Figure 11 compares the predicted arrangement of oxidation states for the MeOH (A or B) and ammonia (C) treated samples based on structure 6 of Figure 1. The binding of the ammonia to manganese cluster results in a shift of the Mn(III) from $Mn_A$ (or $Mn_C$) to $Mn_D$, the weakly exchange coupled manganese ion. We show the ammonia binding as a bridge between $Mn_C$ and $Mn_D$. Such an assignment is consistent with ESEEM experiments which predict that ammonia binds to manganese cluster as a bridging ligand.[29]

It is simple to imagine that formation of the $NH_2$ bridge shifts the reduction potential of the Mn ions of the cluster such that the flanking Mn is now the Mn(III). The movement of the Mn(III) ion from the trinuclear core to $Mn_D$ also results in a change in the sign of the zero-field-splitting term from negative to positive. Mn(III) ions with $D < 0$ cm$^{-1}$ have a $^5B_{1g}$ electronic ground state, while Mn(III) ions with $D > 0$ cm$^{-1}$ have an $^5A_1$ electronic ground state.[17,53] It is straightforward to demonstrate that a Mn(III) ion with a $^5B_{1g}$ electron ground state has $A_{iso}$ and $A_{dip}$ $^{55}$Mn hyperfine tensors of opposite sign, while a Mn(III) ion with an $^5A_1$ electronic ground state has $A_{iso}$ and $A_{dip}$ $^{55}$Mn hyperfine tensors of the same sign.[53] It is clear from Tables 5 and 6 that our calculated intrinsic isotropic and dipolar $^{55}$Mn hyperfine tensors for MeOH- and ammonia-treated PS II centers have the correct signs for their respective electronic ground states. This correlation of electronic ground state with the hyperfine tensors is an internal check of the robustness of our structural analysis.

A $^5B_{1g}$ Mn(III) ion will have either a square pyramidal five coordinate or a tetragonally elongated six-coordinate ligand environment. A $^5A_1$ Mn(III) ion will have either a trigonal bipyramidal five coordinate or a tetragonally compressed six-coordinate ligand environment. While the magnitude of the isotropic portion of the Mn(III) intrinsic $^{55}$Mn hyperfine tensor should in principle be sensitive to the coordination number, no model compound studies have been performed to determine the extent of this correlation. However, as theoretical studies of the structure and mechanism of the manganese cluster become more sophisticated, our predicted zero-field-splitting and $^{55}$Mn hyperfine tensors should provide useful constraints on the ligand field environments used in these calculations.

**The $g = 4.1$ Signal.** As discussed earlier, there are two CW-EPR signals associated with PS II centers trapped in the $S_2$-state. The first is the multiline signal at $g = 2$ (≈3200 G), and the second is a broad signal located at $g = 4.1$ (≈1700 G). While it is known that the $g = 4.1$ signal also arises from the manganese cluster, its exact magnetic origin is not clear.[27] The majority of spectroscopic studies of this second signal indicate that it results from a $S = 5/2$ paramagnetic center.[54,55] Åhrling et al. have argued based on their dimer model that the $g = 4.1$ signal results from a $S = 3/2$ paramagnetic center.[20] However, we have shown that the Åhrling et al. dimer model is not a valid model for the manganese cluster (vide supra). To date, there has been no attempt to determine if the $g = 4.1$ signal might arise from an $S = 7/2$ spin state.

The relative amounts of the $g = 4.1$ signal to the $g = 2$ signal depend on sample preparation and illumination conditions. Illumination of PS II centers at 200 K results in $g = 4.1$ and $g = 2$ signals of approximately equal intensity. Illumination of PS II centers at 140 K results in the majority of the centers being placed in the $g = 4.1$ form of the manganese cluster.

(53) Campbell, K. A.; Force, D. A.; Nixon, P. J.; Dole, F.; Diner, B. A.; Britt, R. D. *J. Am. Chem. Soc.* **2000**, *122*, 3754−3761.

(54) Boussac, A.; Un, S.; Horner, O.; Rutherford, A. W. *Biochemistry* **1998**, *37*, 4001−4007.

(55) Haddy, A.; Dunham, W. R.; Sands, R. H.; Aasa, R. *Biochim. Biophys. Acta* **1992**, *1099*, 25−34.

Warming of the sample to 200 K results in $g = 4.1$ and $g = 2$ signals of the same intensity as illumination at 200 K. In the presence of alcohol such as methanol and ethanol, the $g = 4.1$ signal intensity is reduced while the $g = 2$ signal intensity is increased. Illumination of PS II centers at 200 K with light whose wavelength is less than 700 nm results in creation of only the $g = 2$ EPR signal.[32] Subsequent illumination with 800 nm light results in conversion of a portion of the $g = 2$ signal into the $g = 4.1$ signal. Boussac et al. have argued that illumination at 800 nm excites a Mn−Mn intervalence band, resulting in a transfer of an electron from a Mn(III) ion to a Mn(IV) ion.

EXAFS experiments indicate that the structure of the manganese cluster giving rise to the $g = 4.1$ form is very similar to the structure of the manganese cluster giving rise to the $g = 2$ form. The only observed change is a lengthening of one of the 2.7 Mn−Mn distances to 2.85 Å.[11] As a result, any structural model for the manganese cluster should be able to accommodate both signals without requiring large changes in structure. It has been pointed out previously that the "dimer of dimers" structures (1−4 in Figure 1) cannot easily accommodate the higher spin needed for the $g = 4.1$ signal.[25,56] However, within our trimer/monomer model it is straightforward to generate an $S = {}^5/_2$ or $S = {}^7/_2$ ground spin state without significant change in the structure of the manganese cluster, as well as to theoretically support the observations of Boussac and co-workers.[32,54] The ground spin state is always $S = {}^1/_2$ regardless of the position of the Mn(III) ion if $J_{CD}$ is antiferromagnetic. $J_{CD}$ must change from an antiferromagnetic coupling to a ferromagnetic coupling to generate a higher spin ground state. The spin will be $S = {}^7/_2$ if the Mn(III) ion is on $Mn_A$, $Mn_C$ or $Mn_D$ but $S = {}^5/_2$ if the Mn(III) ion is on $Mn_B$. We show the geometry of the preferred $S = {}^5/_2$ spin state in Figure 11D. If the Mn(III) ion had previously resided on $Mn_C$ and NIR illumination results in its movement to $Mn_A$ or $Mn_B$ then the change in the sign of the $J_{CD}$ coupling is possible to explain. The exchange pathway between $Mn_C$ and $Mn_D$ is mediated by the overlap of the metal orbitals with those of the oxygen bridge. The change in the oxidation state of $Mn_C$ will result in a change in the character of the metal orbitals of the $Mn_C$ ground state and could therefore change the sign of the exchange coupling between $Mn_C$ and $Mn_D$.

**$S_0$-State.** Since the $S_0$-state is two-electron reduced from the $S_2$-state, it should have an odd number of electrons and potentially a ground spin state of $S = {}^1/_2$ with a CW-EPR spectrum centered near $g = 2$. Two groups have recently reported an $S_0$-state CW-EPR signal with resolved $^{55}$Mn hyperfine structure centered near $g = 2$ for PS II centers treated with MeOH.[22,33,57] Messinger and co-workers[33] show that a CW-EPR signal centered at $g = 2$ is present in the absence of MeOH but that the $^{55}$Mn hyperfine structure is significantly reduced. Åhrling et al.[57] propose that a single Mn(II,III) unit is responsible for the $S_0$-state CW-EPR spectrum but provide no spectral simulations to support this proposal. This idea seems largely based on the dinuclear Mn(III,IV) $S_2$-state model proposed earlier by Åhrling and Pace.[20,21] Given that the $^{55}$Mn ENDOR appears to rule out this dinuclear model and that the $S_0$-state EXAFS shows a similar $S_0$-state structure as for the $S_1$ and $S_2$-state,[58] we prefer to concentrate on tetranuclear models for the $S_0$-state spin system.

On the basis of spectral simulations of the CW-EPR spectrum of the $S_0$-state as well as XANES and EXAFS experiments on the $S_0$-state, Messinger and co-workers predict that the manganese cluster in the $S_0$-state consists of four manganese nuclei, with a valence assignment of Mn(II,III,IV,IV) or Mn(III,III,III,IV). They discuss the $S_0$-state spectrum in the context of the "dimer-of-dimers" model.[33] Although they report projection matrices to support their structural assignment and either valence assignment, they do not report the exchange couplings, $J_{jk}$, used to calculate these projection matrices. We have not been able to reproduce the projection matrices reported by Messinger and co-workers for either the Mn(II,III,IV,IV) or Mn(III,III,III,IV) valence assignments without assigning ferromagnetic couplings within the di-$\mu$-oxo bridged Mn−Mn units in the "dimer of dimers" structure. However, such an assignment violates our earlier assumption 3, that such couplings should be strongly antiferromagnetic. We are however able to generate the projection matrices reported by Messinger and co-workers for both the Mn(II,III,IV,IV) and Mn(III,III,III,IV) valence assignments using our trimer/monomer "dangler" structural model. Figure 12 depicts the valence assignments consistent with the projection matrices reported by Messinger and co-workers.[33] We have begun to perform our own simulations of the $S_0$-state CW-EPR signal, but as yet we cannot determine which valence assignment yields the best simulation. Such a determination will most likely require ESE-ENDOR experiments similar to what we have reported for the $S_2$-state (vide supra). We do consider it significant, given the structural similarities of the $S_0$ and $S_2$-states as described by EXAFS,[11,58] that the trimer−monomer model appears able to readily account for the $S_0$-state magnetic properties.

## Conclusions

We have performed a series of CW-EPR and ESE-ENDOR experiments on untreated, MeOH-treated, and ammonia-treated PS II centers trapped in the $S_2$-state. Through simultaneous simulation of both the CW-EPR and ESE-ENDOR data sets we demonstrate that four $^{55}$Mn hyperfine tensors are needed to properly simulate the available data. We demonstrate that previous analyses of the CW-EPR data previously performed by other researchers are not fully compatible with our ESE-ENDOR data. We present a structural model for the manganese cluster that is not only consistent with the CW-EPR and ESE-ENDOR data but is also consistent with the $S_2$ oxidation state [3 Mn(IV) and 1 Mn(III)] inferred from XANES experiments and the Mn−Mn distances derived from EXAFS experiments.[11−15]

As shown in Figure 10, our model predicts that the manganese cluster consists of a strongly antiferromagnetically coupled trinuclear core, with a fourth more weakly exchanged coupled manganese ion in close proximity. In MeOH-treated PS II centers, the Mn(III) ion can be at either end of the trinuclear core. We propose that binding of ammonia to the manganese cluster results in a $NH_2$ bridge formation between the trinuclear core and the adjacent monomer manganese, with the Mn(III) ion now on the monomer manganese. Furthermore, we demonstrate that our model is capable of predicting the existence of the $g = 4.1$ signal of the $S_2$-state as well as the proposed oxidation state rearrangement brought about by NIR illumination of samples trapped in the $S_2$-state. The trinuclear−monomer model is also capable of describing the $S_0$-state magnetics.

(56) Pecoraro, V. L.; Hsieh, W.-Y. In *Metal Ions in Biological Systems*; Sigel, A., Sigel, H., Eds.; Marcel Dekker: New York, 2000; pp 429−504.
(57) Åhrling, K. A.; Peterson, S.; Styring, S. *Biochemistry* **1997**, *36*, 13148−13152.
(58) Messinger, J.; Robblee, J. H.; Fernandez, C.; Cinco, R. M.; Visser, H.; Bergmann, U.; Glatzel, P.; Cramer, S. P.; Campbell, K. A.; Peloquin, J. M.; Britt, R. D.; Sauer, K.; Yachandra, V. K.; Klein, M. P. In *Photosynthesis: Mechanisms and Effects*; Garab, G., Eds.; Kluwer: Dordrecht, 1998; pp 1279−1282.

This study clearly shows the power of ENDOR spectroscopy applied to magnetic metal nuclei of a paramagnetic cluster. First, as shown in Figure 9, ENDOR spectroscopy provides an immediate test for any simulation of a CW-EPR field swept spectrum. Second, it is the ability of ESE-ENDOR to accurately measure the hyperfine matrices that makes it possible to make specific predictions as to zero-field-splitting parameters and arrangement of oxidation states.

As mentioned above, Hasegawa et al.[19] propose a distorted cubane model based on the trinuclear/monomer motif. While Zheng and Dismukes[17] do not provide much discussion concerning the trinuclear/monomer motif, they do clearly state that such a structure is consistent with the analysis of their CW-EPR data. While we feel the effective $^{55}$Mn hyperfine tensors used by these two groups in their spectral analysis are not as accurate as the tensors we present in Table 4, their work nonetheless demonstrates the robustness of the trinuclear/monomer motif as a structure for the manganese cluster of PS II. Furthermore, Semin and Parak have proposed a trinuclear/monomer structure based on sequence homology with diiron-oxo enzymes.[59] Recently, Siegbahn has performed a series of density functional calculations aimed at determining the mechanism of the oxygen evolving complex.[60,61] In these calculations, he finds that a satisfactory geometry for the manganese cluster in the $S_2$-state resembles that shown in Figure 11B.[61]

Although we are not unique in proposing a trinuclear/monomer model, our ESE-ENDOR data and spectral analysis provide the strongest experimental foundation and most accurate magnetic model that together can serve as a reliable starting point for further application of the trinuclear/monomer model to other S-states where the experimental record is less complete. A reliable starting point is important in light of the DFT structures of Siegbahn[61] and the eagerly awaited X-ray structure of photosystem II.[62,63] The DFT calculations are constrained by the activation energies for each of the S-state transitions and may be more sensitive to the differences in structure between the various S-states than the absolute structure of a particular S-state. While we can anticipate high-resolution PS II X-ray structures revealing the coordinates of the OEC, at least initially these structures will be only of the dark stable $S_1$-state. At this point, using the detailed $S_1$ structure as a basis, the DFT calculations and the EPR/ENDOR data will provide accurate electronic and physical structures of $S_2$. Additionally, $^{55}$Mn ENDOR experiments being carried out on the $S_0$-state should open this most reduced state of the cluster to the same level of characterization, and continued progress in EPR characterization of the integer spin $S_1$[23,24,64,65] and $S_3$[66,67] states hold much promise for characterization of these states of the OEC cluster as well.

(59) Semin, B. K.; Parak, F. *FEBS Lett* **1997**, *400*, 259−262.
(60) Siegbahn, P. E. M.; Crabtree, R. H. J. *J. Am. Chem. Soc.* **1999**, *121*, 117−127.
(61) Siegbahn, P. E. M. *Inorg. Chem.* **2000**, *39*, 2923−2935.
(62) Zouni, A.; Lüneberg, C.; Fromme, P.; Schubert, W. D.; Saenger, W.; Witt, H. T. In *Photosynthesis: Mechanisms and Effects*; Garab, G., Eds.; Kluwer: Dordrecht, 1998; pp 925−928.
(63) Kuhl, H.; Kruip, J.; Seidler, A.; Krieger-Liszkay, A.; Bunker, M.; Bald, D.; Scheidig, A. J.; Rögner, M. *J. Biol. Chem.* **2000**, *275*, 20652−20659.
(64) Dexheimer, S. L.; Klein, M. P. *J. Am. Chem. Soc.* **1992**, *114*, 2821−2826.
(65) Yamauchi, T.; Mino, H.; Matsukawa, T.; Kawamori, A.; Ono, T.-A. *Biochemistry* **1997**, *36*, 7520−7526.
(66) Matsukawa, T.; Mino, H.; Yoneda, D.; Kawamori, A. *Biochemistry* **1999**, *38*, 4072−4077.
(67) Ioannidis, N.; Petrouleas, V. *Biochemistry* **2000**, *39*, 5246−5254.
(68) Cinco, R. M.; Rompel, A.; Visser, H.; Aromi, G.; Christou, G.; Sauer, K.; Klein, M. P.; Yachandra, V. K. *Inorg. Chem.* **1999**, *38*, 5988−5998.

**Acknowledgment.** We dedicate this paper to the memory of Dr. Melvin P. Klein, whose contributions to our understanding of photosynthetic oxygen evolution have greatly inspired each of us. Support was provided by NIH (GM48242) to R.D.B.

## Appendix I

A spin system consisting of one $S = {}^1/_2$ electron spin coupled to four $I = {}^5/_2$ $^{55}$Mn nuclear spins results in a Hamiltonian matrix of order 2592. An eigenvalue problem of this size cannot be addressed through normal matrix diagonalization techniques, and researchers typically make use of second-order perturbation theory expressions generated from the Hamiltonian of eq A1.

$$\hat{H}_{\text{coupled}} = \vec{B}\cdot\tilde{g}'\cdot\hat{S}_T + \sum_i^n [\hat{S}_T\cdot\tilde{A}_i'\cdot\hat{I}_i + \hat{I}_i\cdot\tilde{P}_i\cdot\hat{I}_i - \gamma_i\vec{B}\cdot\hat{I}_i] + \hat{S}_T\cdot\tilde{D}'\cdot\hat{S}_T \quad \text{(A1)}$$

Although second-order perturbation theory is quite adequate for simulating the CW-EPR spectra of spin systems with hyperfine constants up to 300 MHz, this approach is not always adequate for simulating ENDOR data of spin systems with such large hyperfine constants. Although we do not need such large hyperfine constants to simulate the $S_2$ EPR signal of PS II, it is important that our simulation program be robust enough that we can sample a sufficiently large amount of parameter space to ensure we do not miss an opportunity to better simulate our data. Furthermore, with hyperfine constants on the order of 300 MHz, second-order perturbation theory can underestimate the $^{55}$Mn nuclear transition frequencies by as much as 5 MHz. This could translate into an underestimation of the hyperfine coupling constant by as much as 10 MHz. While this may appear to be a small error, it is our goal to provide the most accurate analysis of the CW and ENDOR data possible.

For an $S = {}^1/_2$ spin system, in the limit where the electron Zeeman term is significantly larger than the other terms in the Hamiltonian, the hyperfine, quadrupole and nuclear Zeeman terms can be thought of as perturbations of the electron Zeeman term, and the eigenvalues of the Hamiltonian in eq A1 can be written as shown in eq A2. where the $E(M_{Ii})$ are perturbation

$$E(M_S, M_{I1}, M_{I2}, M_{I3}, M_{I4}) = E(M_S) + E(M_{I1}) + E(M_{I2}) + E(M_{I3}) + E(M_{I4}) \quad \text{(A2)}$$

corrections for the individual $^{55}$Mn nuclei and $E(M_S) = g\beta\vec{H}\cdot\hat{S}$. Typically, the values of $E(M_{Ii})$ are calculated using second-order perturbation theory. However, it is possible to rewrite eq A2 to permit use of matrix diagonalization. First, since the electron Zeeman energy does not depend on the perturbation corrections and there are no significant magnetic interactions between the manganese nuclei, eq A2 can be rewritten as eq A3.

$$E(M_S, M_{I1}, M_{I2}, M_{I3}, M_{I4}) = E(M_S) + E(M_S, M_{I1}) - E(M_S) + E(M_S, M_{I2}) - E(M_S) + E(M_S, M_{I3}) - E(M_S) + E(M_S, M_{I4}) - E(M_S) \quad \text{(A3)}$$

In this equation, $E(M_S,M_i) = E(M_S) + E(M_{Ii})$ and represents the energy levels of an $S = {}^1/_2$, $I = {}^5/_2$ spin system. With eq A3, our original spin system (one $S = {}^1/_2$ electron spin, four $I = {}^5/_2$ nuclear spins) has been transformed to four independent ($S = {}^1/_2$ electron spin, $I = {}^5/_2$ nuclear spin) systems. Equation A3 does not mean that the four manganese ions of the cluster

each have a $S = {}^1/_2$ electron spin. This transformation is only a mathematical convenience.

Our original Hamiltonian in eq A1 is now represented by five different Hamiltonians. One Hamiltonian for each ($S = {}^1/_2$, $I = {}^5/_2$) system given by eq A4 and a fifth Hamiltonian for the Zeeman energy given by eq A5. Diagonalization of A4 and A5 will yield the $E(M_S,M_{Ii})$ and $E(M_S)$ energy values needed to solve eq A3.

$$E(M_S, M_{Ii}) \equiv \hat{H}(S,I_i) = \vec{B}\cdot\tilde{g}'\cdot\hat{S} + \hat{S}\cdot\tilde{A}_i'\cdot\hat{I}_i + \hat{I}_i\cdot\tilde{P}_i\cdot\hat{I}_i - \gamma_i\vec{B}\cdot\hat{I}_i \quad \text{(A4)}$$

$$E(M_S) \equiv \hat{H}(S) = \vec{B}\cdot\tilde{g}'\cdot\hat{S} \quad \text{(A5)}$$

**Eigenvector Reconstruction.** In addition to obtaining the 2592 eigenvalues, $E(M_S, M_{I1}, M_{I2}, M_{I3}, M_{I4})$, of the Hamiltonian in eq A1, it is also necessary to obtain the 2592 eigenvectors, $|M_S, M_{I1}, M_{I2}, M_{I3}, M_{I4}>$. The eigenvector of the ($S = {}^1/_2$, four $I = {}^5/_2$) spin system is the tensor product of the individual spin eigenvectors as shown in eq A6:

$$|M_S, M_{I1}, M_{I2}, M_{I3}, M_{I4}> = |M_S>\otimes|M_{I1}>\otimes|M_{I2}>\otimes|M_{I3}>\otimes|M_{I4}> \quad \text{(A6)}$$

If the Zeeman term of eq A1 is the dominant term, eq A6 can be rewritten as eq A7:

$$|M_S, M_{I1}, M_{I2}, M_{I3}, M_{I4}> = |M_S>\otimes|M_S>\otimes|M_{I1}>\varnothing|M_S>\otimes|M_S>\otimes|M_{I2}>\varnothing|M_S>\otimes|M_S>\otimes|M_{I3}>\varnothing|M_S>\otimes|M_S>\otimes|M_{I4}>\varnothing|M_S> \quad \text{(A7)}$$

which then be rewritten as eq A8:

$$|M_S, M_{I1}, M_{I2}, M_{I3}, M_{I4}> = |M_S>\otimes|M_S, M_{I1}>\varnothing|M_S>\otimes|M_S, M_{I2}>\varnothing|M_S>\otimes|M_S, M_{I3}>\varnothing|M_S>\otimes|M_S, M_{I4}>\varnothing|M_S> \quad \text{(A8)}$$

where the $|M_S, M_{Ii}>$ terms are the eigenvectors of the separate Hamiltonians given by eq A4 and the $|M_S>$ terms are the eigenvectors of eq A5. Examination of the equations shows that in eq A6, $|M_{Ii}> = |M_S, M_{Ii}>\varnothing|M_S\rangle$.

The eigenvectors for the $S = {}^1/_2$, 4 $S = {}^5/_2$ system are then reconstructed as follows:

$$|M_S = +, M_{I1}, M_{I2}, M_{I3}, M_{I4}> = a|M_S' = \frac{1}{2}> \prod_{k=1}^{4} \frac{\sum_{j=-5/2}^{5/2} e_{kj}|M_S' = \frac{1}{2}, M_{kj}' = j>}{a|M_S' = \frac{1}{2}>} + b|M_S' = -\frac{1}{2}> \prod_{k=1}^{4} \frac{\sum_{j=-5/2}^{5/2} f_{kj}|M_S' = -\frac{1}{2}, M_{ki}' = j>}{b|M_S' = -\frac{1}{2}>} \quad \text{(A9)}$$

$$|M_S = -, M_{I1}, M_{I2}, M_{I3}, M_{I4}> = c|M_S' = \frac{1}{2}> \prod_{k=1}^{4} \frac{\sum_{j=-5/2}^{5/2} e_{kj}|M_S' = \frac{1}{2}, M_{kj}' = j>}{c|M_S' = \frac{1}{2}>} + d|M_S' = \frac{-1}{2}> \prod_{k=1}^{4} \frac{\sum_{j=-5/2}^{5/2} f_{kj}|M_S' = \frac{-1}{2}, M_{kj}' = j>}{d|M_S' = \frac{-1}{2}>} \quad \text{(A10)}$$

where

$$|M_S = +> = a|M_S' = \frac{1}{2}> + b|M_S' = -\frac{1}{2}>$$
$$|M_S = -> = c|M_S' = \frac{1}{2}> + d|M_S' = -\frac{1}{2}> \quad \text{(A11)}$$

and

$$|M_S = \frac{1}{2}, M_{Ii}> = \sum_{j=-5/2}^{5/2} e_j|M_S' = \frac{1}{2}, M_{Ii}' = j> + \sum_{j=-5/2}^{5/2} f_j|M_S' = -\frac{1}{2}, M_{Ii}' = j> \quad \text{(A12)}$$

The primed eigenvectors represent the basis set prior to diagonalization, and the unprimed eigenvectors represent the bases set following diagonalization. The *a*, *b*, *c*, and *d* constants are determined by diagonalization of the Zeeman Hamiltonian,

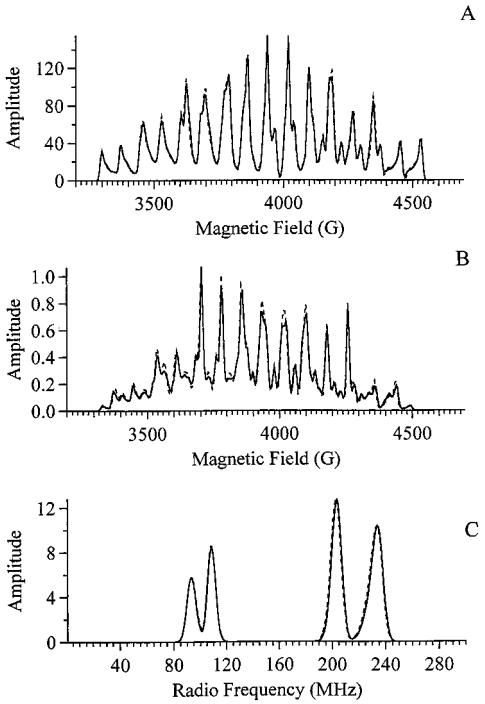


**Figure 13.** Comparison of the calculated ESE-EPR field swept and ESE-ENDOR spectra using the simulations parameters in Table 3 for compound A performed with a full matrix diagonalization (solid line) or with the separate diagonalization method given in Appendix 1. (A) Calculation performed for perpendicular polarization of applied and static magnetic fields; (B) calculation performed for parallel polarization of applied and static magnetic fields; (C) comparison of the calculated ESE-ENDOR spectra at a field of 3300 G.

eq A5. The $e_j$ and $f_j$ constants are determined by diagonalization of the Hamiltonian for the *i*th separate spin system, eq A4.

For the case of a dinuclear Mn(III,IV) system, we can make a numerical comparison of our separate diagonalization method to that of a full matrix diagonalization approach. Figure 13A shows the calculated perpendicular polarization EPR field swept spectrum for a Mn(III,IV) dimer using the parameters in Table 3 from the simulation of compound A. The solid trace was calculated by diagonalizing the full 72 × 72 Hamiltonian matrix for a Mn(III,IV) dimer. The dashed trace was calculated by performing a separate diagonalization of a ($S = {}^1/_2$, $I = {}^5/_2$) spin system for the Mn(III) and the Mn(IV) ions and then reconstructing the eigenvalues and eigenvectors of the ($S = {}^1/_2$, 2 $I = {}^5/_2$) spin system using eqs A3, A9, and A10. It is quite clear that the two methods yield nearly identical results. Figure 13B shows the calculated parallel polarization EPR field swept spectrum for the same Mn(III,IV) dimer using the parameters in Table 3. Again, it is clear that the spectrum reconstructed from separate diagonalizations is almost an exact reproduction of the spectrum calculated using the true diagonalization method. Given the data shown in Figure 13, we feel that using the separate diagonalization method we can reproduce transition probabilities to an accuracy of at least 1% if not 0.1%. Figure 13C shows the results of calculating the ENDOR spectrum at a field position of 3300 G using full matrix diagonalization and our separate diagonalization method. The two spectra are exactly the same with respect to frequency and identical to within 0.1% in terms of intensity.

In the final analysis, the $^{55}$Mn hyperfine and quadrupole tensors used in oursimulation of the $S_2$-state EPR data in Figures 5 and 8 are sufficiently small that our separate diagonalization method does not yield improved accuracy over second-order perturbation theory. However, we feel the method will find utility in the analysis of systems where the hyperfine or quadrupole tensors are sufficiently large that perturbation theory becomes unusable. We have found the separate diagonalization method to be particularly useful in simulating spectral features at field values between 800 and 2000 G. In this field region, perturbation theory becomes inaccurate even for relatively small values of the hyperfine tensors.

JA002104F